Predictive Modelling of Hydrate Formation and Dissociation

M. Wapperom

Technische Universiteit Delft

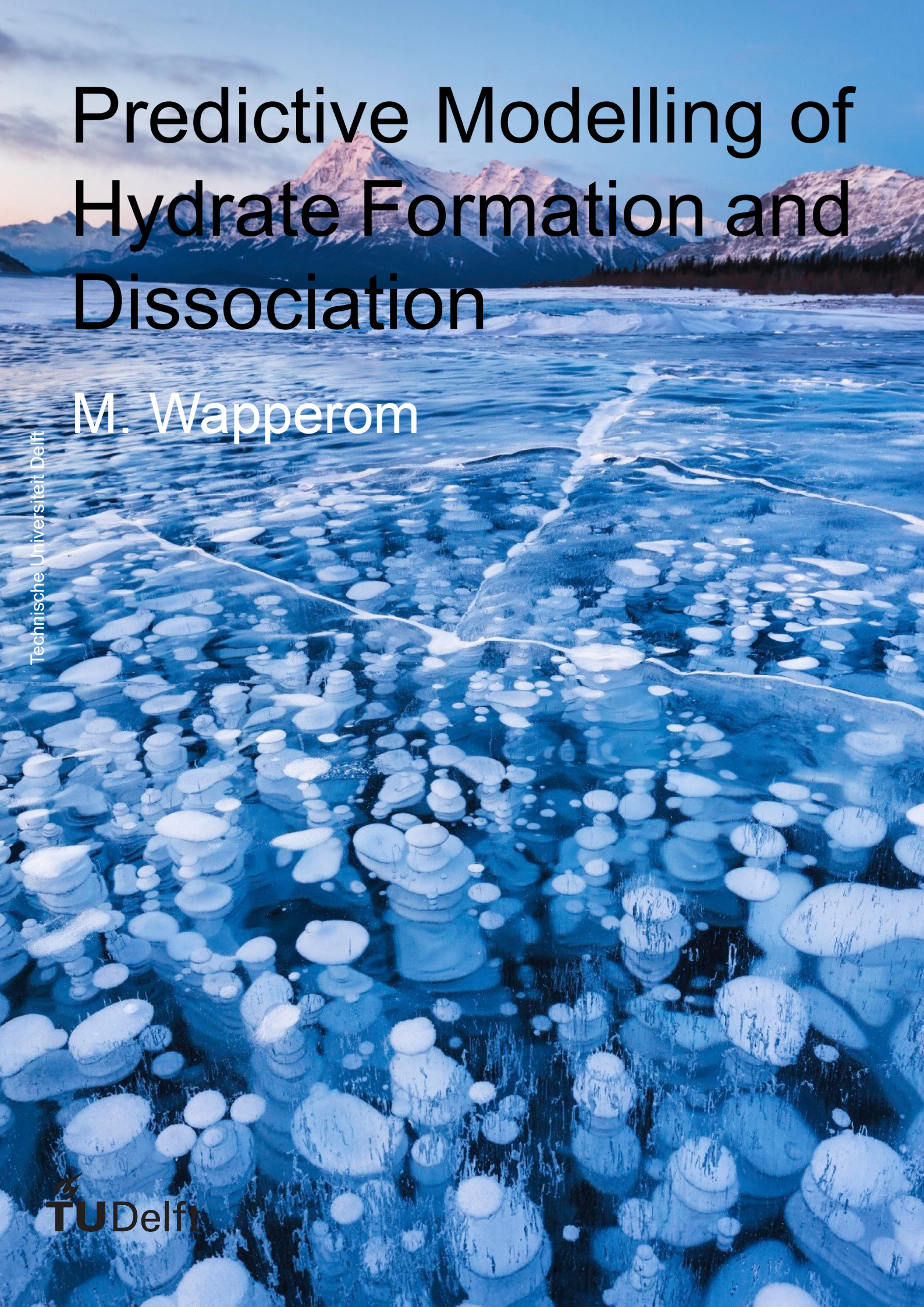

TU Delft

Predictive Modelling of Hydrate Formation and Dissociation

by

Michiel Wapperom

to obtain the degree of Master of Science
at the Delft University of Technology,
to be defended publicly on Monday November 25, 2019 at 2:00 PM.

Student number:	4280628	
Project duration:	December 1, 2018 – November 25, 2019	
Thesis committee:	Dr. D.V. Voskov,	TU Delft, supervisor
	Dr. K.H.A.A. Wolf,	TU Delft
	Dr. P.J. Vardon,	TU Delft
	Dr. G. Ersland,	University of Bergen
	X. Lyu,	TU Delft

An electronic version of this thesis is available at `http://repository.tudelft.nl/`.

Cover image after [13]

TU Delft

Abstract

Natural gas hydrates are often considered as a hazard in hydrocarbon production and pipeline transport, but are also recognized as a potential energy resource. Naturally occurring hydrate deposits exist under suitable conditions of low temperature and high pressure, typically in shallow marine sediments and in and below the permafrost, and may host large quantities of recoverable natural gas. Besides, the process of exchanging hydrate guest molecules potentially offers the added benefit of storage of carbon dioxide, as CO_2-hydrates are, under typical conditions, thermodynamically more stable than CH_4-hydrates.

Several short-term field pilots have been undertaken, but the longer term dynamics of natural gas hydrate reservoirs remain unclear. Core-scale experiments performed at the University of Bergen were designed to provide essential data for field-scale numerical simulation of hydrate formation, dissociation and guest molecule exchange processes. Implementation of experimental findings into a simulator for hydrate-bearing formations may lead to a better understanding of the dynamics of hydrate-bearing geologic media and, in turn, to more effective strategies for commercial use of hydrate reservoirs. This thesis describes the development of an extension of the DARTS general-purpose reservoir simulator for hydrate-bearing reservoirs. The complexity of such systems can be effectively captured using the operator-based linearization approach and experimentally observed behaviour of hydrate systems can be implemented and matched with relative ease. This enables the combination of conventional conservation equations with the use of complex physics and empirical models.

The existing DARTS-framework has been extended to include a kinetic description of the hydrate formation and dissociation reaction. Ultimately, a non-isothermal model has been tested for 1-D formation and dissociation cases. Comparison of results with literature shows similar behaviour and trends. The effect of water salinity has also been captured by the model, which has to be validated with experimental results. However, further development of the model is required in order for the model to be able to match measured data.

Preface

The call for climate solutions is becoming urgent these days. The world's growing population combined with its habit of pursuing economic growth is interfering with the physical boundaries of our planet. Despite the undisputed value Earth has to the economic system, economic policy often fails to address environmental issues appropriately. However, there is an increasing need for suitable measures and technology that provide the desired mitigating effect. During my time as an undergraduate student, I felt that the faculty of Geosciences is a place where you can be at the frontier of shaping Earth's future. Even though I chose to follow the track focusing on Petroleum Engineering after that, I knew that the traditional oil industry was not what I wanted to be in. It was back then and it will continue to be my ambition to work on solutions to minimize the damage that society does to our planet.

Finishing off my Master's has been quite a task. The thesis work involved many aspects covered during the MSc track, as well as areas of thermodynamics and chemical engineering. The subject of gas hydrates is as challenging as it is exciting. I came across the topic in a lecture by Dr. Voskov, who would later be my supervisor. I was fascinated by the certain elusiveness that surrounds hydrates, and the fact that hydrate research is still in its pioneering stage. But above all, it provided me with a research topic that covers subjects that have grabbed my interest during my studies and matches my ambitions in climate-related technology.

After a long time familiarizing with the subject and spending a while in Norway at the University of Bergen, it turned out that I actually had to deal with everything Denis had foreseen at the start of the project. I would like to thank you for the right guidance at the right time. The development of the model was put on the fast track once we started implementing our findings into the existing DARTS-framework. Whenever I faced any issues, Xiaocong was always ready to take some time to fix them, no matter what time it was or how busy you were. Finally, I can't forget to thank the people in Norway. My time in Bergen has helped me really understand and get a feel for the topic of gas hydrates, many thanks to Geir, Stian and the UiB for this opportunity and their willingness to support my research. Hopefully this project will be the start of a productive collaboration in this area.

Lastly, I would like to show my appreciation for family and friends, always ready to express their support and confidence in me. In particular, my parents have always shown their gracious warmth and support and have even made an attempt to become familiar with the physics behind my model... My brother has his own ways of giving support with humour and subtle self-mockery, but I always feel the appreciation from his side. Finally, my uncle, aunts and grandma have always been able to put my efforts into perspective and remind me of the achievements I could be proud of when the project was getting tough, ultimately bringing this thesis to what it has become.

Michiel Wapperom
Delft, November 2019

Contents

List of Figures

List of Tables

1

Introduction

Natural gas hydrates are often considered as a hazard in hydrocarbon production and pipeline transport, but are also recognized as a potential energy resource. These clathrate hydrates are crystalline solids composed of hydrogen-bonded water, stabilized by small non-polar guest molecules. Naturally occurring hydrate deposits exist under suitable conditions of low temperature and high pressure, typically in shallow marine sediments and in and below the permafrost, and may host large quantities of recoverable natural gas. Besides, the process of exchanging hydrate guest molecules potentially offers the added benefit of storage of carbon dioxide, as CO_2-hydrates are, under typical conditions, thermodynamically more stable than CH_4-hydrates.

Several short-term field pilots have been undertaken, but the longer term dynamics of natural gas hydrate reservoirs remain unclear. Additional experimental and numerical investigation has been launched to better understand the results of field data, mostly focusing on issues related to permeability alteration in the presence of hydrates and the interaction between the hydrate and guest molecules. Core-scale experiments performed at the University of Bergen [2, 3, 8] were designed to provide essential data for field-scale numerical simulation of hydrate formation, dissociation and guest molecule exchange processes.

Numerical simulations are essential for the development of subsurface reservoirs. Simulators present a numerical solution of the equations that describe the physical processes of interest on a mesh representing the porous formation, imitating the behaviour of a real system (distribution of pressure and temperature, components, etc.). Reservoir simulators are widely used for performance evaluation, sensitivity studies and optimization of development strategies. A simulator for hydrate-bearing formations may lead to a better understanding of the dynamics of hydrate-bearing geologic media and, in turn, to more effective strategies for commercial use of hydrate reservoirs.

There is a persistent demand for accurate and efficient models and, especially in ensemble optimization, which requires thousands of simulations, the performance of a simulator is a primary issue. In order to increase the accuracy of a model, finer computational grids in space or time can be applied or a more complex description of the governing physics can be used. However, the improvement in accuracy is generally associated with more computationally demanding simulations.

The operator-based linearization approach proposed by Voskov [29] significantly simplifies the implementation of complex simulation frameworks by introducing algebraic operators that capture all complex physics and associated nonlinear terms. It provides the opportunity to represent the exact physics of the simulation problem by approximation interpolants defined at each point in the discrete parameter space from the set of primary unknowns pressure, temperature and composition.

This thesis will describe the development of an extension of the general-purpose reservoir simulator [29] for hydrate-bearing reservoirs. The complexity of such systems can be effectively captured using the operator-based linearization approach and experimentally observed behaviour of hydrate systems can be implemented and matched with relative ease. This enables the combination of conventional conservation equations with the use of complex physics and empirical models. Ultimately, the predictive model can be constrained to experimental data and can be used to support further experimental and numerical research.

1.1. Background

1.1.1. Description of gas hydrate systems

Naturally occurring hydrate deposits exist where the thermodynamic conditions allow hydrate formation: under suitable conditions of low temperature and high pressure, with an adequate supply of gas. A small non-polar molecule (e.g., CH_4, CO_2, N_2; most often CH_4) will react with water to form hydrates. Hydrates are concentrated in two distinctly different types of geological formations where the necessary low temperatures and high pressures exist: in the permafrost and in shallow marine sediments [26].

The stability region of hydrates is controlled by pressure and temperature gradients (Figure 1.1). As pressure increases and water temperature decreases with depth, the conditions in a shallow part below the seafloor or in the permafrost may allow for stable hydrates. The lower depth limit of hydrate deposits is controlled by the geothermal gradient [26]. Moreover, hydrates need a sufficient supply of gas. For methane hydrates, the source can be from thermogenic or biogenic origin. In hydrate-bearing pores, the effective porosity and permeability decreases due to the fractional filling of the pore space with hydrates, preventing gas from migrating upwards and leading to a trap under which free gas can accumulate [7]. On seismic, this is often characterized by a sharp reflection cross-cutting sedimentary strata, referred to as a bottom-simulating reflector, or BSR. The BSR due to gas hydrates are caused by the negative acoustic impedance contrast between sediments containing gas hydrates and free gas underneath the gas hydrate stability zone [5].

The formation of hydrates in the pore space has significant implications to the behaviour of flow and transport through the porous medium. The presence of hydrates can significantly reduce the absolute permeability and inherently the ability of fluid phases to flow. Moreover, the inclusion of solid hydrate in the pore space reduces the relative permeability of mobile phases compared to a system with no hydrates present, even with similar mobile phase saturations [3]. This is believed to be related to the nature of hydrate growth, which, for water-wet formations, has been shown to occur along the gas-water interface. This potentially blocks flow paths for the mobile phases after hydrate formation, increasing the immobile saturation of fluid phases [1, 3].

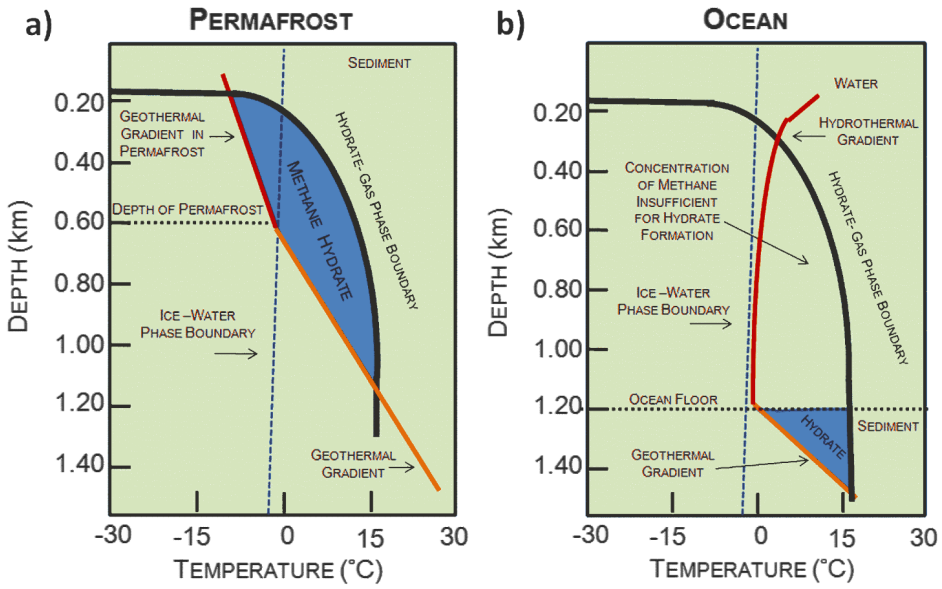

Figure 1.1: Methane hydrate stability zone, after [9]. (Credit: S.E. Harrison, Stanford University)

1.1.2. Relevance of gas hydrates

Potential energy resource Natural gas hydrates are recognized as a promising future energy resource. Based on assessment of potentially recoverable volumes of in-place resources, it seems likely that global gas hydrate resources that occur as high-concentration deposits within sand-rich reservoirs are substantial, perhaps on the order of tens of thousands of tera cubic feet [16].

Methane production from hydrates can be achieved by facilitating thermodynamic conditions in which the hydrate is not stable. Three main methods to destabilize the hydrate are depressurization, thermal stim-

ulation and inhibitor injection. Of these methods, depressurization is often regarded as the most viable strategy for methane recovery from hydrates. However, for all of these methods, production of gas is associated with vast amounts of water and removing the hydrate from consolidated sediments may compromise the structural integrity of the geologic formations [16].

Another method that can be used for methane recovery is the direct exchange of hydrate guest molecules with more stable hydrate formers (e.g. CO_2). This method allows for in-situ exchange of the hydrate guest molecule above hydrate equilibrium conditions [8] and offers a way to extract CH_4 from hydrate bearing sediments without destabilizing the formation [16] and potentially the ability for long term storage of CO_2. However, the retention of solid hydrate will limit the ultimate reservoir permeability and therefore, production-utilising exchange processes may be inferior to depressurization in terms of potential gas flow rates [16].

Potential carbon sequestration The process of CH_4-CO_2 exchange in hydrates [8] has the potential of being a viable strategy for thermodynamically stable long term CO_2-sequestration, with the added benefit of associated natural gas production, without destabilizing the formation [16].

Possible impact on global climate Rising surface and water temperatures due to global warming might pose a threat to climate-sensitive hydrate deposits. The synergy between warming climate and gas hydrate dissociation raises concerns that global warming could result in the release of large quantities of methane from destabilized hydrate accumulations in marine and permafrost settings. Some hypotheses suggest a positive feedback between modern climate change and the release of methane from dissociating gas hydrates and paleoclimate studies have implicated such a feedback during past global warming events [25].

1.1.3. Previous work

Numerical studies on the simulation of gas hydrate systems are limited. Moridis [20] has developed the TOUGH+ HYDRATE simulator, which is capable of simulating methane hydrate formation and dissociation under kinetic and equilibrium conditions, involving the various production techniques destabilizing the hydrate. Yonkofski [31] has made an attempt to develop and demonstrate kinetic models representing the $CH_4/CO_2/N_2$ guest molecule exchange process that is presumed to have occurred during field tests. Qorbani [24] has incorporated a full kinetic description of competing hydrate phase transitions through Gibbs' free energy minimization, as opposed to the simplified description of kinetic mechanisms that proceed to equilibrium.

1.2. Objectives and workflow

In this work, a predictive simulation model will be developed for gas hydrates formation and dissociation, based on core-scale experimental results. The newly developed chemical branch of the Delft Advanced Research Terra Simulator (DARTS) will be utilized for these purposes. First, chemical models of hydrate formation and dissociation based on kinetic reactions will be reviewed and implemented. Here, it is the aim to describe the formation and dissociation of methane hydrates under varying pressure, temperature and composition. The effect of water salinity on hydrate behaviour is accounted for in thermodynamic models. Advanced porosity-permeability relations [3] will be implemented. The simulation model will be applied by reproducing experimental and numerical results [14, 30] and the predictive model can ultimately be constrained to the measured data.

1.3. Outline

This thesis will follow the development of an extension of the DARTS general-purpose simulator [29] for hydrate-bearing systems. Section 2 describes the theoretical framework behind the model, outlining the modelled processes and assumptions, followed by a description of governing physics and numerical techniques. Section 3 discusses all physical properties required for input to the model. Results for 1-D test cases are presented in Section 4. Sections 5 and 6 discuss the results, limitations to the model and possible improvements.

2

Model description

In this chapter, the theoretical framework behind the model is described. First, a brief description of the model is given and modelled processes and assumptions are outlined. Then, the equations that govern fluid flow in porous media are presented, followed by a discussion of operator-based linearization, the numerical technique that can be used to solve these governing equations.

2.1. Description of the model

2.1.1. Components and phases

In a simple methane-hydrate system, the components considered are CH_4, H_2O and NaCl dissolved in water. Methane hydrates are non-stoichiometric substances, that is, it has no set chemical composition. The pseudo-reaction for hydrate formation is described by

$$CH_4 + n_H H_2O \longrightarrow CH_4 \cdot n_H H_2O \tag{2.1}$$

where n_H denotes the hydration number, equal to the number of water molecules bound to each guest molecule. Full cage occupancy of sI-hydrate corresponds to 8 CH_4 molecules per 46 H_2O molecules, yielding a hydration number of 5.75. A more detailed description of cage occupancy and hydration numbers is given in Appendix B.2.2.

The model describes the formation and dissociation of sI-type methane hydrates under kinetic conditions. For a problem involving kinetic hydrate formation or dissociation, hydrates are considered an individual component according to the reaction described in (2.1); under equilibrium conditions, hydrate would not be treated as an individual component, but simply as a state of the CH_4-H_2O system. The mass components are partitioned among three possible phases j: aqueous Aq, vapour V and solid-hydrate H. Note that, under kinetic conditions, hydrate is both a component and a phase. Under equilibrium conditions, hydrate would be treated only as a phase. A more detailed description will be given in Section 2.2.2.

2.1.2. Modelled processes and underlying assumptions

The aim is to model the following physical processes in hydrate-bearing geologic systems:

1. Partitioning of the mass components (CH_4, H_2O and NaCl) among the possible phases (V, Aq)
2. The advective flow of vapour and aqueous phases in the porous medium
3. Heat exchanges due to advection and conduction
4. The formation and dissociation of methane hydrates under kinetic conditions
5. The implications of hydrate growth for flow
6. The effects of salinity on hydrate behaviour

Some simplifying assumptions have been made in the development of the underlying physical, thermodynamic and mathematical model:

1. Darcy's law is valid in the simulated domain under the conditions of the study
2. Instantaneous local thermodynamic equilibrium between V and Aq phases
3. Simplified phase thermal properties; no heat related to reactions
4. Dissolved salts are only present in the aqueous phase, i.e. do not precipitate
5. Diffusion, gravity and capillary pressure effects are neglected
6. Mechanical dispersion is neglected
7. Rock matrix is incompressible

2.2. Governing equations

A non-isothermal hydrate system can be fully described by the appropriate mass and energy balance equations, provided with appropriate initial and boundary conditions. For each independent variable, one equation needs to be solved. For a system containing n_c components, this leads to $n_c - 1$ equations for composition, one equation for pressure and one equation for temperature: a total of $n_c + 1$ equations for each grid block. In addition, the partitioning of mass components among different phases is described by the set of thermodynamic relations.

2.2.1. Mass and energy balance equations

The simulation domain of a hydrate system has been subdivided into discrete grid blocks. Mass is conserved in each grid block according to

$$\frac{\partial}{\partial t}\int_{V_n} M^i \, dV = -\int_{\Gamma_n} F^i \cdot \mathbf{n} \, dA + \int_{V_n} q^i \, dV \tag{2.2}$$

Here, M^i, F^i and q^i denote the accumulation-, flux- and source-sink terms for each component i, respectively, where

$$M^i = \sum_j \phi \rho_{mj} s_j x_{ij}$$

$$F^i = \sum_j x_{ij} \rho_{mj} u_j$$

$$q^i = \sum_j x_{ij} \rho_{mj} \hat{q}_j + v_{i,k} r_k$$

with $\hat{q}_j$ the phase sourcerate per unit volume and r_k describing the behaviour of the hydrate under kinetic conditions (please refer to Section 2.2.2) and velocity described by Darcy's law:

$$u_j = -\frac{k_{r,j}\mathbf{k}}{\mu_j}\left(\nabla P_j - \rho_j \mathbf{g}\right) \tag{2.3}$$

Saturation is defined as the volumetric fraction occupied by a particular phase. This is obtained by the relation:

$$s_j = \frac{v_j/\rho_{mj}}{\sum_{n_p} v_k/\rho_{mk}} \tag{2.4}$$

Using the divergence theorem, this can be translated into the conservation equation for mass (2.5) for each component, similar to Kala [11]:

$$\frac{\partial}{\partial t}\left(\sum_j \phi \rho_{mj} s_j x_{ij}\right) = -\nabla \cdot \left(\sum_j x_{ij} \rho_{mj} \mathbf{u}_j\right) + \sum_j x_{ij} \rho_{mj} q_j + v_{i,k} r_k \qquad i = 1, ..., n_c \tag{2.5}$$

Energy is tracked in a similar manner. The accumulation term contains contributions from the pore fill as well as from the rock matrix. The flux of heat includes the transport of heat through advection and conduction. Energy sources are either associated with mass sources or heat sources and also include heat released

or consumed in the hydrate formation or dissociation reaction. Translating this into accumulation, flux and source terms for heat θ equivalent to the mass conservation terms gives

$$M^{\theta} = \phi \sum_j \rho_{mj} s_j U_j + (1-\phi) U_r$$

$$F^{\theta} = \sum_j h_j \rho_{mj} u_j + \overline{\kappa} \nabla T$$

$$q^{\theta} = \sum_j h_j \rho_{mj} \hat{q}_j + Q_r$$

with

$$Q_r = r_k \Delta H^0$$

In our assumptions, we set the heat related to reactions equal to zero. Then, the conservation equation for energy can be written in the same form as for mass, yielding:

$$\frac{\partial}{\partial t}\left(\phi \sum_j \rho_{mj} s_j U_j + (1-\phi) U_r\right) = -\nabla \cdot \left(\sum_j h_j \rho_{mj} u_j + \overline{\kappa} \nabla T\right) + \sum_j h_j \rho_{mj} \hat{q}_j \tag{2.6}$$

2.2.2. Thermodynamic relations

In a multiphase system, an exact thermodynamic equilibrium is required at every nonlinear iteration in the molar formulation. To resolve phase behaviour, thermodynamic relations must be solved simultaneously in the nonlinear loop. Here, we describe the procedures for calculating phase behaviour under both kinetic and equilibrium conditions.

Due to the instantaneous local equilibrium assumption, phase behaviour calculations are decoupled from flow and transport. The set of thermodynamic relations described by (2.7) must be simultaneously solved for the conditions of pressure, temperature and composition in each grid block.

$$z_i - \sum_{j=0}^{n_p-1} x_{ij} v_j = 0, \qquad i = 1, ..., n_c \tag{2.7a}$$

$$\sum_{i=1}^{n_c} z_i - 1 = 0, \tag{2.7b}$$

$$\sum_{i=1}^{n_c} (x_{i0} - x_{ij}) = 0, \qquad j = 1, ..., n_p - 1 \tag{2.7c}$$

$$\sum_{j=0}^{n_p-1} v_j - 1 = 0, \tag{2.7d}$$

$$f_{i0}(P, T, \mathbf{x}_0) - f_{ij}(P, T, \mathbf{x}_j) = 0, \qquad i = 1, ..., n_c, \quad j = 1, ..., n_p - 1 \tag{2.7e}$$

where (2.7a) and (2.7b) define overall composition and the composition constraint, respectively; (2.7c) and (2.7d) define phase composition and the overall phase fraction constraint and (2.7e) describes the fugacity constraint which is based on equal fugacity of a particular component across different phases. The fugacity constraint is derived from equal chemical potential in each phase and is described in more detail in Section 3.1. The system of equations in (2.7) can be solved using the negative flash procedure as described by Iranshahr.

A hydrate system can be modelled under kinetic or equilibrium conditions. For kinetic assumptions, the hydrate phase is assumed not to be in equilibrium with the other phases. The hydrate phase is excluded from phase calculations and formation or dissociation of hydrates is driven by the difference in fugacity between phases in order to restore equilibrium. Reaction rates are defined explicitly and are added to the conservation equations. A more detailed description of reaction rates under kinetic conditions is given in Section 3.4. On the contrary, under equilibrium conditions, the hydrate phase is included in the flash calculations. The formation reaction and dissociation reaction occur at an equal rate; reaction rates are not explicitly defined as reactions are assumed to be in equilibrium instantaneously.

2.3. Nonlinear formulation and operator-based linearization

2.3.1. Nonlinear formulation

The governing equations (2.5) and (2.6) are solved for pressure, temperature and overall composition. For a system with n_c components, this leads to a set of $n_c - 1$ independent variables for composition and two additional variables for pressure and temperature: $\{P, T, z_1, ..., z_{n_c-1}\}$. This yields a total of n_c mass balance equations and one energy balance equation for each grid block. In order to solve this system of equations, the equations are discretized in space and time using the Fully Implicit Method (FIM) with two-point flux approximation and upstream weighting [29]. After application of a finite-volume discretization and backward Euler approximation in time, the residual form of the mass balance equation (2.5) for component i reads

$$r_{i,m} = V\Big[\Big(\sum_j \phi\rho_{mj}s_j x_{ij}\Big)^{n+1} - \Big(\sum_j \phi\rho_{mj}s_j x_{ij}\Big)^{n}\Big] - \Delta t\sum_l \Big(\sum_j x_{ij}^l \rho_{mj}^l \Gamma_j^l \Delta\psi^l\Big)^{n+1} - \Delta t\Big(\sum_j x_{ij}\rho_{mj}q_j + \upsilon_{i,k}Vr_k\Big)^{n+1} = 0 \quad (2.8)$$

where $q_j = \hat{q}_j V$ is the volumetric source rate. Here, $\Gamma_j^l = \Gamma^l k_{r,j}^l/\mu_j^l$ denotes the phase transmissibility, where $\Delta\psi^l$ is the potential difference over boundary l between grid blocks a and b and Γ^l denotes the constant geometrical part of transmissibility over l, including permeability and the geometry of the control volume for any (un)structured grid:

$$\Gamma^l = \frac{\alpha_a\alpha_b}{\alpha_a+\alpha_b} \text{ where } \alpha_m = A_l k_m/D_m \quad (2.9)$$

where A_l is the surface area of boundary l, k_m is the permeability in grid block m and D_m denotes the distance between boundary l and the centre of grid block m.

In a similar manner, the residual form of the energy balance equation (2.6) reads

$$r_{\theta,m} = V\Big[\Big(\phi\sum_j \rho_{mj}s_j U_j + (1-\phi)U_r\Big)^{n+1} - \Big(\phi\sum_j \rho_j s_j U_j + (1-\phi)U_r\Big)^{n}\Big] - \Delta t\sum_l \Big(\sum_j h_j^l \rho_{mj}^l \Gamma_j^l \Delta\psi^l + \Gamma_c^l\overline{\kappa}\Delta T^l\Big)^{n+1} - \Delta t\Big(\sum_j h_j\rho_{mj}q_j\Big)^{n+1} = 0 \quad (2.10)$$

Here, Γ_c^l corresponds to the conductive transmissibility, which includes thermal conductivity of all phases, including rock and the geometry as $\Gamma_c^l = \frac{\alpha_a\alpha_b}{\alpha_a+\alpha_b}$ where $\alpha_m = A_l/D_m$.

The mass and energy conservation equations described here contain secondary variables that depend on the values of nonlinear unknowns at the current time step. This introduces nonlinearity into the system. In addition, the assumption of instantaneous thermodynamic equilibrium requires a multiphase flash procedure (the system described by the thermodynamic relations in Section 2.2.2) for each grid block. Once multiphase flash is solved to obtain phase fractions υ_j and composition of each phase x_{ij} at the given conditions for the given composition, the solution to the system of the mass and energy balance equations (2.5) and (2.6) can be found by converging to a solution of all variables such that all $n_c + 1$ residuals for each grid block described by (2.8) and (2.10) are equal to zero. This can be obtained by using the Newton-Raphson method. At every iteration, residuals and a Jacobian - containing derivatives of all residuals with respect to all independent unknowns - must be constructed. This step is called linearization. For every nonlinear iteration, the following linear system of equations is solved:

$$J(y^k)(y^{k+1} - y^k) = -r(y^k) \quad (2.11)$$

where $J(y^k)$ and $r(y^k)$ are the Jacobian and residual defined at a nonlinear iteration k. Vector y contains nonlinear unknowns pressure, temperature and mole fractions of $n_c - 1$ components. The primary unknowns are updated with every iteration. When the residual falls within the pre-defined tolerance, the system has converged [29].

2.3.2. Operator-based linearization

The Newton-Raphson approach requires the partial derivatives of the residuals with respect to all independent variables, implying that it also needs the derivatives of secondary variables with respect to the primary nonlinear unknowns. This may require the solution of a highly nonlinear system, where the nonlinear solver

has to resolve all of the small features of the property descriptions, which can be quite challenging and is often unnecessary due to the numerical nature and uncertainties in property evaluation [29].

The operator-based linearization approach by Voskov [29] significantly simplifies the implementation of complex simulation frameworks by introducing algebraic operators that capture all complex physics and nonlinear terms. Instead of keeping track of each property and its derivatives with respect to nonlinear unknowns, abstract algebraic operators representing the physics can be constructed and assembled into the set of Jacobian and residuals defined at each iteration.

2.3.3. Operator form of the conservation equations and construction of operators

The operator-based linearization approach has been described for general purpose reservoir simulation by Voskov [29]. In this section, the parameterization of the governing equations will be described and physics-based operators will be generated. For a more detailed description of the method, the reader is referred to Voskov [29].

In order to apply the described approximation method, we rewrite the residual equations described in Section 2.3.1, representing each term as a product of state-dependent (ω) and space-dependent operators (ξ). The resulting mass conservation equation for commponent i in grid block m is

$$r_{i,m} = a_i(\xi)\big(\alpha_i(\omega) - \alpha_i(\omega_n)\big) - \sum_l b_i(\xi,\omega)\beta_i(\omega) - c(\xi)\gamma_i(\omega) - d(\xi)\theta_i(\omega) = 0 \qquad i = 1,...,n_c \tag{2.12}$$

where

$$a(\xi) = \phi V(\xi) \tag{2.13a}$$
$$\alpha_i(\omega) = \sum_j \rho_{mj} s_j x_{ij} \tag{2.13b}$$
$$b(\xi,\omega) = \Delta t \Gamma^l(\xi)\big(P^b - P^a\big) \tag{2.13c}$$
$$\beta_i(\omega) = \sum_j x^l_{ij} \rho^l_{mj} \frac{k^l_{r,j}}{\mu^l_j} \tag{2.13d}$$
$$c(\xi)\gamma_i(\omega) = V \Delta t v_{i,k} r_k(\omega) \tag{2.13e}$$
$$d(\xi)\theta_i(\omega) = \Delta t \sum_j x_{ij} \rho_{mj} q_j(\xi,\omega,\mathbf{u}) \tag{2.13f}$$

The modified energy conservation equation in grid block m becomes

$$r_{\theta,m} = a_\theta(\xi)\big(\alpha_\theta(\omega) - \alpha_\theta(\omega_n)\big) - \sum_l \Big(b_\theta(\xi,\omega)\beta_\theta(\omega) + c_\theta(\xi,\omega)\gamma_\theta(\omega)\Big) - \theta_\theta(\xi,\omega,\mathbf{u}) = 0 \tag{2.14}$$

where

$$a_\theta(\xi)\alpha_\theta(\omega) = a_{\theta,f}(\xi)\alpha_{\theta,f}(\omega) + a_{\theta,r}(\xi)\alpha_{\theta,r}(\omega)$$
$$c_\theta(\xi,\omega)\gamma_\theta(\omega) = c_{\theta,f}(\xi,\omega)\gamma_{\theta,f}(\omega) + c_{\theta,r}(\xi,\omega)\gamma_{\theta,r}(\omega)$$

and

$$a_{\theta,f}(\xi)\alpha_{\theta,f}(\omega) = \phi V(\xi) \sum_j \rho_{mj} s_j U_j \tag{2.15a}$$
$$a_{\theta,r}(\xi)\alpha_{\theta,r}(\omega) = (1-\phi) V(\xi) U_r \tag{2.15b}$$
$$b_\theta(\xi,\omega) = \Delta t \Gamma^l(\xi)\big(P^b - P^a\big) \tag{2.15c}$$
$$\beta_\theta(\omega) = \sum_j h^l_j \rho^l_{mj} \frac{k^l_{r,j}}{\mu^l_j} \tag{2.15d}$$
$$c_{\theta,f}(\xi,\omega)\gamma_{\theta,f}(\omega) = \Delta t \phi \Gamma^l(\xi)(T^b - T^a)\overline{\kappa_f} \tag{2.15e}$$
$$c_{\theta,r}(\xi,\omega)\gamma_{\theta,r}(\omega) = \Delta t (1-\phi) \Gamma^l(\xi)(T^b - T^a)\overline{\kappa_r} \tag{2.15f}$$
$$d(\xi,\omega,\mathbf{u})\theta_\theta(\omega) = \Delta t \sum_j h_j \rho_{mj} q_j(\xi,\omega,\mathbf{u}) \tag{2.15g}$$

This introduces operators α_i, β_i, γ_i and θ_i for each mass component and α_θ, β_θ, γ_θ and θ_θ for energy. In this form, the nonlinear system is defined only in terms of physical state-dependent operators. The values of these operators are uniquely determined in the parameter space of the simulation problem with the set of primary unknowns $\{P, T, z_1, ..., z_{n_c-1}\}$. Approximation interpolants are generated at each point in the discrete parameter space at the pre-processing stage and stored in (n_c+1)-dimensional tables. Alternatively, this approach was modified to adaptively evaluate the operators during simulation, improving the overall performance of the system greatly. During simulation, operator values for a specific state are obtained by multilinear interpolation of tabulated values. Partial derivatives required for the assembly of the Jacobian matrix can be evaluated directly from the tables.

It must be noted here that, generally, heat related to any reactions is accounted for in the energy conservation equation, but since this is ignored in our assumptions, this term reduces to zero and there is no need for the additional operator.

The units for each operator and variable that must be specified in DARTS are listed in Appendix A.

2.4. Summary and relationship to following sections

In this section, the governing equations describing the modelled physics have been introduced and numerical simulation techniques to solve these equations have been set out. For each grid block, a set of n_c+1 equations must be solved to calculate all independent variables: $\{P, T, z_1, ..., z_{n_c-1}\}$. Fully implicitly solving the governing equations in space and time using the operator-based linearization scheme requires the introduction of operators that capture the nonlinear terms that describe the physics. Approximation interpolants for the operators are generated and stored in (n_c+1)-dimensional tables. During simulation, a solution at a particular time step is found using the Newton-Raphson method. Residual and Jacobian can be constructed with the described operators. Operator values are obtained by multilinear interpolation of tabulated values. Partial derivatives can be evaluated directly from the tables.

In the next sections, physical properties and behaviour of hydrate systems will be described. This will be used as input to the model. All input data used in the governing equations will be described in Section 3. It will first discuss general physical properties related to compositional transport in a hydrate system and then cover specific issues related to hydrate formation and dissociation and its implications to the behaviour and flow through the system that have to be determined from empirical models and experiments. Section 4 will then describe the test cases for 1-D, comparing the results with literature. Section 5 will discuss the assumptions and limitations, some of which might be relaxed upon further development of the model.

3

Physical properties

This section describes the physical properties associated with gas hydrate systems that need to be defined in order to build a simulation model. First, phase behaviour is calculated using the negative flash procedure with successive substitution iteration (SSI). Then, thermophysical properties are defined in order to provide input for the mass conservation equations. Next, permeability relationships for hydrate systems are described. Finally, models for hydrate formation and dissociation reaction rates are reviewed.

3.1. Phase behaviour

Due to the instantaneous local equilibrium assumption, phase behaviour calculations are decoupled from flow and transport. Under kinetic conditions, the present phases are assumed not to be in equilibrium with the hydrate phase H. Phase calculations are performed on all phases except for the hydrate phase and phase partitioning is calculated using negative flash as described by Iranshahr [10] with successive substitution iteration. Under equilibrium conditions, the hydrate phase is included in the flash procedure.

3.1.1. Negative flash

Iranshahr [10] developed a method to resolve multiphase thermodynamic equilibrium (2.7) based on a generalized negative-flash strategy, for which no phase-stability test is required. The negative-flash procedure for multiphase systems with constant K-values is formulated in Iranshahr (2010). The overall mole fraction of a component z_i in equation (2.7a) can be written as:

$$z_i = x_{i0}\upsilon_0 + \sum_{j=1}^{n_p-1} x_{ij}\upsilon_j \qquad \text{for i} = 1,...,n_c \tag{3.1}$$

where one phase is arbitrarily chosen as the 'base' phase, which is denoted by index 0. Using relation (2.7d) and constant K-values as:

$$\upsilon_0 = 1 - \sum_{j=1}^{n_p-1} \upsilon_j \tag{3.2}$$

$$x_{ij} = K_{ij}x_{i0} \qquad \text{for i} = 1,...,n_c \text{ ; for j} = 1,...,n_p-1 \tag{3.3}$$

the relation for z_i in (3.1) can be rewritten as:

$$z_i = x_{i0}\Big(1 + \sum_{j=1}^{n_p-1} \upsilon_j(K_{ij}-1)\Big) = x_{i0}m_i(\mathbf{v}) \qquad \text{for i} = 1,...,n_c \tag{3.4}$$

where

$$m_i(\mathbf{v}) = 1 + \sum_{j=1}^{n_p-1} \upsilon_j(K_{ij}-1)$$

In order to determine the equilibrium partitioning of all components among all phases, one must solve the following coupled $N_p - 1$ objective functions:

$$f_j(\mathbf{v}) = \sum_{i=1}^{n_c}(x_{i,0} - x_{i,1}) = \sum_{i=1}^{n_c}\frac{z_i(1-K_{i,j})}{m_i(\mathbf{v})} = 0 \qquad \text{for j} = 1,...,n_p-1 \tag{3.5}$$

The negative-flash algorithm combines Successive Substitution Iteration (SSI) with the Newton method. During any SSI iteration, the K-values are assumed constant. As the K-values describe the distribution of components among phases, all unknown mole fractions of the base phase x_{i0} can be calculated from the set of phase fractions v_j according to (3.4) and then all other unknown mole fractions x_{ij} can be derived from the distribution coefficients K_{ij} (3.3). The work flow for the negative-flash procedure is described in Figure 3.1. Then fugacity coefficients are updated according to the fugacity models described in the next section, in order to obtain new K-values.

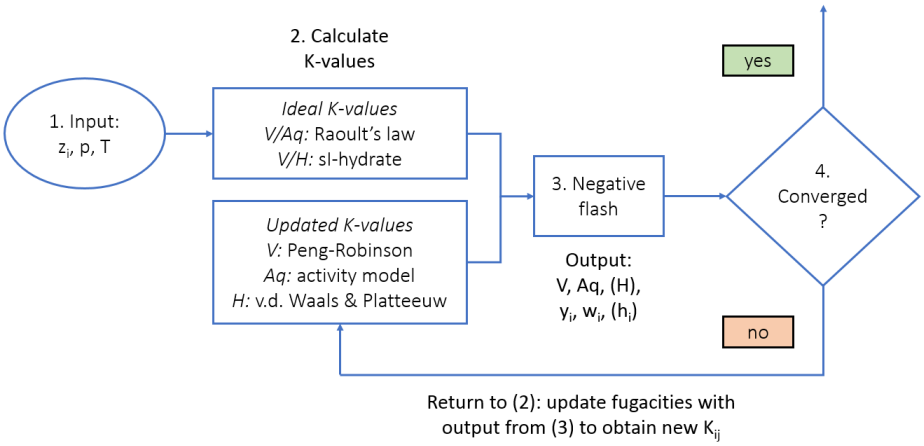

Figure 3.1: Work flow for the negative-flash procedure

3.1.2. Fugacity models

In equation (3.5), K-values describe the distribution of components between phases. This follows from the fugacity constraint from equation (2.7), which can be rewritten as:

$$\frac{f_{i0}}{f_{ij}} = \frac{x_{i0}\phi_{i0}P}{x_{ij}\phi_{ij}P} = 1 \qquad \text{for i} = 1,...,n_c \text{ ; for j} = 1,...,n_p - 1 \tag{3.6}$$

from which the relation for K-values can be derived as used in (3.3):

$$K_{ij} = \frac{\phi_{i0}}{\phi_{ij}} = \frac{x_{ij}}{x_{i0}} \tag{3.7}$$

For a system consisting of more than one phase, the equilibrium distribution of a chemical component between phases is characterized by equal chemical potential. However, absolute values of the chemical potential cannot be measured [19]. Fugacity is a measure of the chemical potential μ_{ij}. The fugacity of any component in the desired phase j can be expressed as:

$$f_{ij} = f_{i0} \exp\left[\frac{\mu_{ij} - g_{i0}}{RT}\right] \tag{3.8}$$

where f_{i0} is the ideal gas fugacity of component i at 1 bar, which is simply equal to 1 bar, and g_{i0} denotes the Gibbs energy of component i in the ideal gas state [4]. Fugacity expresses the non-ideal behaviour of a gas. It is equal to the pressure that a pure, ideal gas or the partial pressure that a component in a mixture of ideal gases would need to have for the chemical potential to be equal to the real gas [19]. If the gas is an ideal gas, its fugacity is equal to its pressure [4]. When the fugacities of a chemical in two phases are unequal, transfer of the chemical from the high fugacity phase to the low fugacity phase will occur, until fugacities are equal and equilibrium exists [19].

In order to initiate the negative flash procedure, composition-independent ideal K-values provide an initial guess of phase fractions. Then, based on the output of the first iteration (phase fractions and composition of each phase), fugacity coefficients are updated to obtain new K-values.

Salt is assumed to be present only in the aqueous phase. The presence of salt in the aqueous phase affects the fugacity of this phase and its molality is consequently taken into account in the updated fugacity model.

However, salt mole fractions are not taken into account in negative flash calculations and mole fractions must be normalized before running flash and re-normalized afterwards. Normalization is described in Appendix B.2.3.

Ideal K-values

An initial guess of phase fractions is obtained by solving the set of equations for ideal K-values. Ideal K-values are composition-independent distribution coefficients that are only dependent on component properties, which can be found in B.1.

Vapour and aqueous phases For the ideal distribution coefficient between vapour V and aqueous Aq, we can take the modified Raoult's law as used in Ballard [4], which is described in Appendix B.2.1.

Updated K-values

The fugacity coefficient of each component in each phase must be known to determine the K-values for the next iteration. Several fugacity models are used to calculate fugacity in different possible phases. For fugacities of hydrocarbon phases (vapour V and liquid L), the Peng-Robinson equation of state [22] is used, and for the aqueous phase, an activity-fugacity model is used [32]. Fugacity coefficients are obtained from the models described below, and are used to calculate new K-values according to (3.7). A graphical representation of the negative flash results with the fugacity models used and the implications for methane solubility in the aqueous phase and water in the vapour phase is given in Appendix C.1.

Hydrocarbon phases Fugacity coefficients for vapour and liquid hydrocarbon phases can be obtained from Peng-Robinson equation of state [22], as described in Appendix B.2.2.

Aqueous phase For the aqueous phase, the chemical potential is written in terms of activity rather than fugacity, following the procedure described by Ziabaksh [32]. The method for obtaining fugacity coefficients for components in the aqueous phase is described in Appendix B.2.2.

3.2. Thermophysical properties

The thermophysical properties associated with the mass conservation equations must be specified as input to the model. In this section, models used for phase density and viscosity are discussed. A graphical representation of the thermophysical models used is given in Appendix C.2.

3.2.1. Phase density

Phase density can be measured in molar density $\rho_{m,j}$ and mass density ρ_j. These two density expressions are related through the average molar mass of the phase considered:

$$\rho_{m,j} = \rho_j / M_j \tag{3.9}$$

In the molar formulation of the mass and energy balance equations, all density terms concerned are molar density, except for the gravity term. Moreover, some correlations provide mass density and other properties often require mass density (e.g., viscosity).

Vapour phase Vapour molar density can be derived from the Peng-Robinson EoS with the correction as proposed by Péneloux [23], as described in Appendix B.2.2. Once the roots of equation (B.8) are found, the equation for Z can be rewritten to obtain phase molar density for the V phase:

$$V_{m,j} = \frac{Z_j RT}{P} \qquad \text{for j = V} \tag{3.10}$$

Aqueous phase Solutes dissolved in water significantly affect the density of the aqueous phase. A brine typically contains various dissolved salt species.The other components considered in the model have relatively low concentrations and are not accounted for in density calculations. The mass density of the aqueous phase is calculated using Spivey [27] for the density of a brine and is described in Appendix B.4.1.. Here, it is assumed that the effect of dissolved species is independent of the other dissolved species present in the solution.

Hydrate phase Mass density of the hydrate phase can be calculated according to the relation proposed by Ballard [4], which can be found in Appendix B.4.1.

3.2.2. Phase viscosity

Viscosity describes the resistance of a fluid to shear stress. Viscosity is a function of temperature, pressure and composition.

Vapour phase The method of Lee [15] gives viscosity of typical natural gas mixtures with low non-hydrocarbon content as described in Appendix B.4.2.

Aqueous phase The viscosity of aqueous electrolyte solutions depends strongly on temperature, less on salinity, and is much less dependent on pressure, according to Mao [18].Due to the low solubility of methane, the effect of dissolved CH_4 is neglected. The calculation of the viscosity of brine according to Mao [18] is described in Appendix B.4.2.

3.2.3. Phase thermal properties

In this work, all phase thermal properties are taken as constant over the range of temperature, pressure and composition.

Internal energy If heat is added to a system with constant volume, the heat added is equal to the change in internal energy of the system. The accumulation term in (2.6) contains contributions for specific internal energy of each phase, as well as the rock matrix, as described by:

$$U_t = \phi \sum_j \rho_j s_j U_j + (1-\phi) U_r \tag{3.11}$$

Values for specific internal energy for all phases and rock matrix are given in Appendix B.4.3.

Enthalpy The advective term in (2.6) contains specific enthalpy h_j of each phase. The absolute value of enthalpy cannot be measured, but it is more convenient to consider the change in enthalpy. For processes under constant pressure, the change in specific enthalpy of a phase is equal to total energy change per mole, made up of internal energy and the amount of work required to establish its volume and pressure:

$$h_j = U_j + PV_m = U_j + P/\rho_{mj} \tag{3.12}$$

Values for specific enthalpy for each phase are presented in Appendix B.4.3.

Thermal conductivity The conductive term in (2.6) requires composite thermal conductivity of the medium-fluid ensemble. The same form as used in Yin [30] is implemented here:

$$\overline{\kappa} = \kappa_d + \left(s_{Aq}^{1/2} + s_H^{1/2}\right)\left(\kappa_w - \kappa_d\right) \tag{3.13}$$

where subscripts d and w refer to thermal conductivity of sand under dry and fully saturated conditions, respectively. Values can be found in Appendix B.4.3.

3.3. Permeability and relative permeability

The presence of hydrate in the pore space has significant implications for permeability. The relationships for permeability must take into account the reduction in ability of fluid phases to flow when hydrates are present. Also, the nature of hydrate growth has implications to residual saturations and consequently must be incorporated in relative permeability models.

3.3.1. Permeability and the presence of hydrates

An accurate understanding of hydrate growth patterns is crucial developing a relation for effective permeability alteration in response to the presence of hydrates. In making permeability predictions, the pore-scale hydrate growth habit is a determining factor. Almenningen [1] states that the assumption of either pore-filling

or pore-coating hydrate growth is too simplistic and that the permeability evolution is highly influenced by heterogeneous growth.

Experiments at the University of Bergen [3] show relative permeabilities to liquid CO_2 or CH_4 gas in sandstone cores in a three-phase system (hydrate, gas and brine) and in a two-phase system (gas and brine). Relative permeability was found to be consistently higher in the two-phase system without hydrates than in the three-phase system with hydrates present. The inclusion of solid hydrate in the pore space reduces the relative permeability to gas compared to the two-phase system, even at constant gas saturation. This reduction in relative permeability is believed to be related to an increase of immobile gas after hydrates have formed, as clusters of gas become less interconnected due to the presence of solid hydrate. Almenningen [3] further demonstrated less difference between two-phase and three-phase systems for higher gas saturations. The effective permeability turned out to be more sensitive to hydrate formation at low gas saturations, most likely because the limited vapour phase was more prone to become disconnected and capillary immobilized. Moreover, Almenningen [3] found that the actual hydrate saturation had limited effect on the permeability for a given gas saturation. For a given gas saturation, the presence of hydrate in addition to brine clearly reduced the effective permeability, but the mutual volumetric proportion between hydrate and brine was insignificant for the effective permeability. Mahabadi [17] argues that, with regard to water, the effect of uniformly distributed hydrate saturation for relative permeability values has only a marginal effect. Relative permeability to water becomes lower with more heterogeneous hydrate growth, because the effect of gas expansion has larger effect on plugging water paths when hydrates are non-uniformly distributed.

The effect of hydrate saturation on permeability has been shown to differ when different porous media is used [3]. The same reduction in permeability Almenningen [3] observed in sandstones is not necessarily true for other rock types with different wetting properties. The relation between permeability and hydrate saturation remains unclear, and there does not exist any general correlation between (relative) permeability and hydrate saturation. The effect of hydrate saturation on gas permeability will vary with the particular hydrate growth pattern and resulting phase distribution within the pores [3].

The proposed empirical correlations for water-wet sandstone cores by Almenningen [3] and Mahabadi [17] are discussed in the next section.

3.3.2. Permeability relationships

Almenningen [3] describes two approaches. The hydrate phase can be either viewed as a phase that occupies part of the pore volume and consequently enters the relative permeability relation, or it can be considered as part of the solid matrix, altering absolute permeability and establishing a two-phase relation for relative permeability of the mobile phases. The latter is considered here.

Absolute permeability In this approach, the reduction in effective permeability due to hydrate is accounted for in the absolute permeability. The permeability of the porous medium is then a function of the effective porosity as:

$$\frac{k}{k_0} = \left(\frac{\phi - \phi_c}{\phi_0 - \phi_c}\right)^n \tag{3.14}$$

where k_0 is the absolute permeability when the porosity is ϕ_0 (that is, no hydrate), ϕ_c is a nonzero critical porosity where the absolute permeability becomes zero, and n is a fitting parameter that is dependent on where hydrate accumulates in the pore space. Almenningen [3] fitted the permeability curves with (3.14). Parameters are given in Appendix B.3.1.

Relative permeability Then, the relative permeability curves for the remaining two phases take the form of Brooks-Corey curves:

$$k_{r,V} = k^0_{r,V}\left(\frac{s_V - s_{V,r}}{1 - s_{Aq,r}}\right)^{n_V} \tag{3.15}$$

where $k^0_{r,V}$ is the end-point relative permeability to gas at residual brine saturation $s_{Aq,r}$. $s_{V,r}$ is residual gas saturation and n_V is a fitting parameter controlling the slope of the curve. For the aqueous phase:

$$k_{r,Aq} = k^0_{r,Aq}\left(\frac{s_{Aq} - s_{Aq,r}}{1 - s_{Aq,r}}\right)^{n_{Aq}} \tag{3.16}$$

where end-point relative permeability to water at residual gas saturation is denoted by $k^0_{r,Aq}$ and n_{Aq} is the fitting parameter for the aqueous phase. Almenningen [3] fitted the permeability curves with (3.15) and Ma-

habadi [17] did so for water relative permeability with (3.16). Mahabadi [17] suggests the use of fitting parameters that change with hydrate saturation. Parameters are listed in Appendix B.3.1.

The Brooks-Corey model with fitting parameters has been displayed in Figure 3.2. Here, the solid lines represent the relative permeability relations for a hydrate-bearing system, as opposed to the relative permeability models for a system with no hydrates (dashed lines). Note that the water saturation on the x-axis denotes the hydrate-normalized water saturation. As absolute permeability is reduced by the presence of hydrate according to (3.14), the effect of hydrates on the ability for fluids to flow is more pronounced than only Figure 3.2.

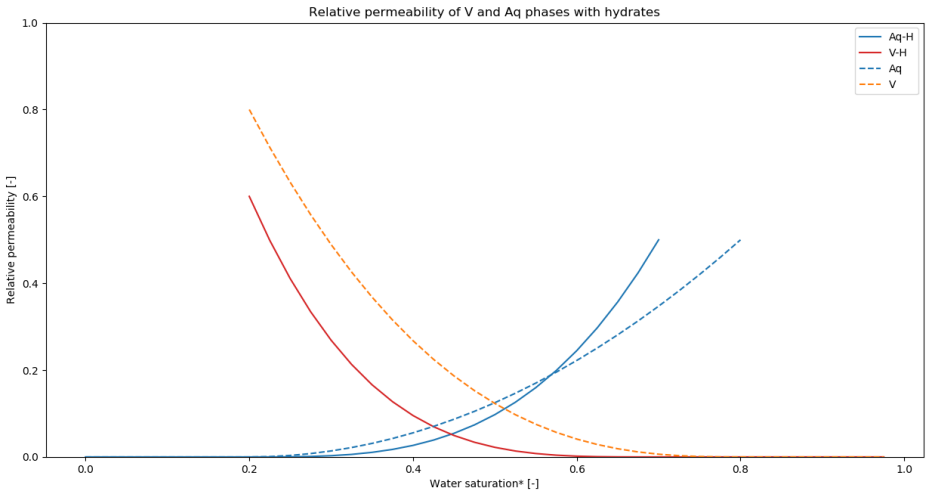

Figure 3.2: Relative permeability models and the effect of hydrate presence

3.4. Hydrate formation and dissociation reactions

Hydrate systems can be modelled either under kinetic or equilibrium conditions, as described in Section 2.2.2. Under equilibrium assumptions, the hydrate phase is incorporated in the negative flash procedure and, consequently, the reaction is assumed to be at its equilibrium instantaneously. When kinetic conditions are considered, the formation or dissociation of hydrates is the result of the hydrate and other phases not being in equilibrium; that is, the fugacity between phases is not equal. In order to restore equilibrium, net transfer of chemicals occurs from the higher fugacity compartment to the lower fugacity compartment. When fugacity of the hydrate phase is lower, hydrates will form; when fugacity of the hydrate is higher, it will dissociate. The difference in fugacity is considered as the driving force behind the hydrate formation or dissociation reaction. The reaction continues until the driving force has reduced to zero at the point where fugacity among phases is equal and equilibrium between the phases has been restored.

The rate of reaction then depends on the magnitude of the driving force and reaction-related parameters. A modified notation of the Arrhenius-type equation for reaction rate as proposed by Kim [12] reads

$$r_k = K A_s \exp\left(\frac{-\Delta E}{RT}\right)(f_{w,H} - f_{w,Aq}) \tag{3.17}$$

where K is the formation or dissociation reaction constant [mol m^{-2} bar^{-1} s^{-1}], A_s is the hydrate surface area [m^2/m^3], ΔE is the activation energy [kJ mol^{-1}] and $(f_{w,H} - f_{w,Aq})$ is the difference in fugacity [bar]. Hydrate fugacity is calculated from Van der Waals-Platteeuw [28] and other phases follow the regular fugacity calculation as described in Appendix B.2.2. The Arrhenius-type exponential term with ΔE a positive number implies that for higher temperatures, the reaction occurs at a faster rate. The reaction constant K must be estimated from matching simulations with experimental results. The calculation of kinetic rate parameters are described in Appendix B.4.4.

The fugacity difference between hydrate and other phases is quantified in Figures 3.3 (effect of gas composition) and 3.4 (effect of pore water salinity), where red indicates dissociation and blue indicates formation.

It can be seen that an unsufficient supply of gas creates a driving force for dissociation, no matter the pressure and temperature conditions (Figure 3.3, upper left) and increasing pore water salinity drives up the stability conditions for hydrates.

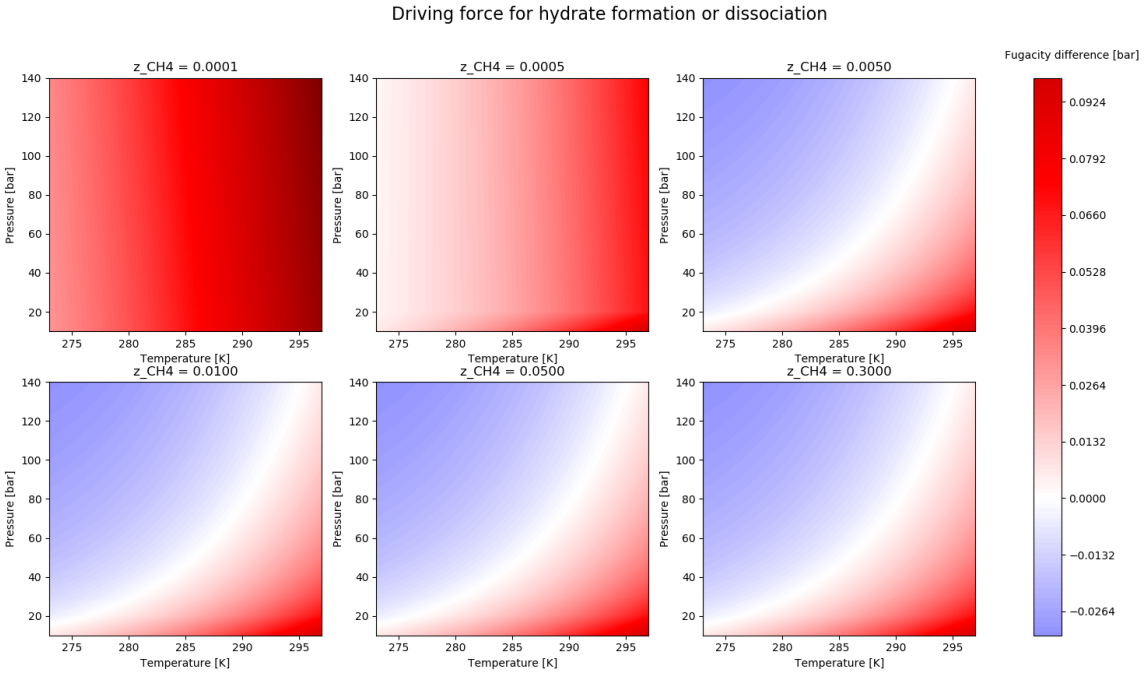

Figure 3.3: Driving force for hydrate formation/dissociation reaction with gas composition; molality = 0

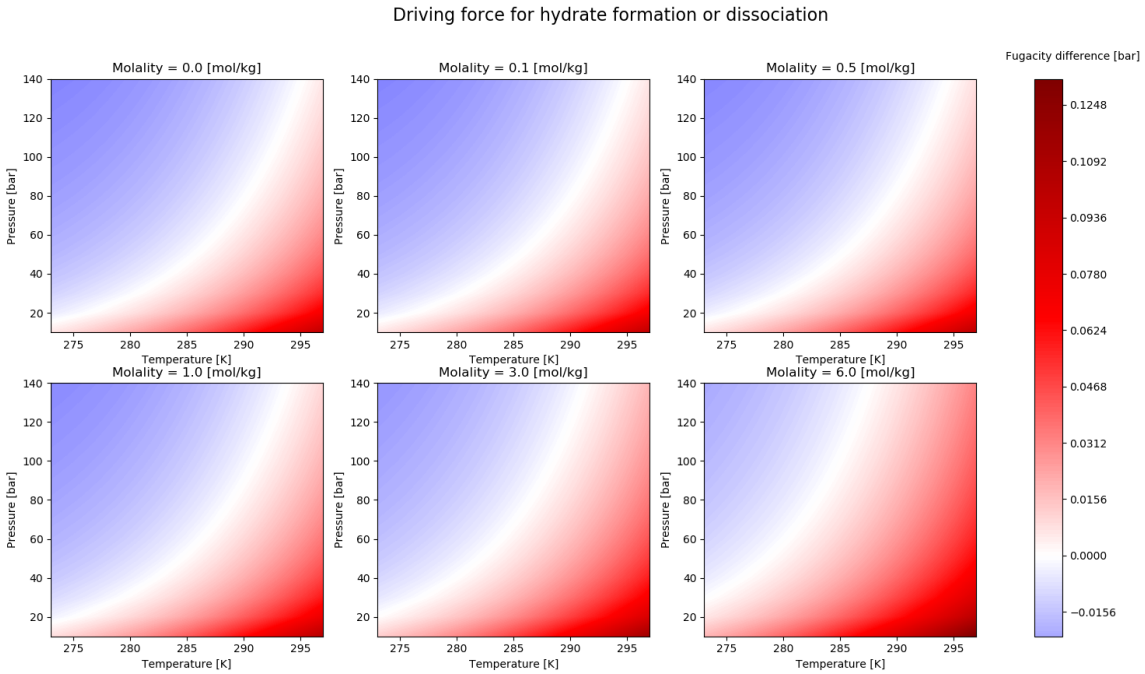

Figure 3.4: Driving force for hydrate formation/dissociation reaction with molality; $z_{CH_4} = 0.05$

4

Results

In this section, results of 1-D test cases are presented. An attempt is made to obtain results for formation and dissociation experiments similar to literature and an extension is made to saline reservoirs.

4.1. Hydrate formation

Yin [30] numerically analysed experimental studies of methane hydrate formation. Here, we run a simulation under similar conditions, with an extension to saline conditions. Results from Yin [30] are shown in Figure 4.1.

Scenario description The reservoir is a small reactor filled with a sandy porous medium. It is first pressurized with methane gas to remove any residual air. After that, water is injected into the reactor up to a saturation of approximately 0.4 (stage I1). The sample is then allowed to stabilize to steady state (stage S1). Pressure and temperature at this point have reached 95 bar and 288 K. Then, the fluid circulating around the reactor is cooled down to a temperature of 274 K, which is sufficiently low to create hydrate-formation conditions (stage F1).

In our simulation run, an attempt is made to obtain results for the F1 stage of this experiment in 1-D. Here, the initial conditions deviate from Yin [30] in that the initial temperature is assumed to be uniform throughout the entire reservoir. The evolution of pressure, temperature, phase saturations and reaction-related parameters through time is tracked. The initial conditions used in the simulation model are given in Table 4.2.

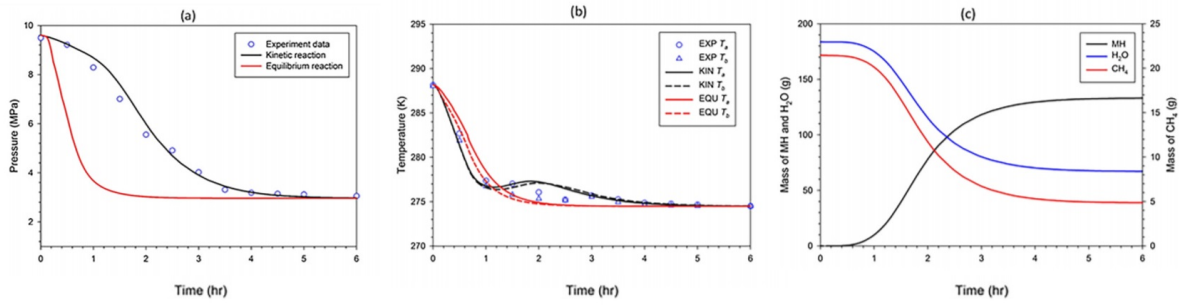

Figure 4.1: Results in Yin [30] with a) pressure evolution, b) temperature evolution and c) mass of each component

Table 4.1: Reservoir description for 1-D formation and dissociation scenarios

Scenario	l_x	n_x	ϕ	k
Formation	50.00	500	0.44	3.93 D
Dissociation	50.00	500	0.30	300 mD

Table 4.2: Initial conditions for 1-D formation scenario similar to Yin [30]

Scenario	$P_{initial}$	$T_{initial}$	z_i			Molality
			CH_4	H_2O	$CH_4 \cdot nH_2O$	
F-274-0	95.00	274.0	0.120	0.880	$1{\cdot}10^{-6}$	0.0
F-274-2	95.00	274.0	0.120	0.848	$1{\cdot}10^{-6}$	2.0
F-278-0	95.00	278.0	0.120	0.880	$1{\cdot}10^{-6}$	0.0
F-278-2	95.00	278.0	0.120	0.848	$1{\cdot}10^{-6}$	2.0

Simulation results The simulation results for the formation scenarios are presented in Figure 4.2 and Figure 4.3. The simulation covers 10 hours after initializing the experiment, allowing the system to equilibrate. Pressure, temperature, composition and hydrate saturation at the end of the simulation are given in Table 4.3.

Under the conditions at the start of each scenario, the fugacity of the fluid phases is higher than that of the hydrate phase. There exists a driving force for hydrate formation as long as the fugacity of all phases is not equal. Water and methane are consumed to form hydrates. The density of hydrate is slightly smaller than water density, resulting in a slight volume increase on this part, but this effect is greatly offset by the reduction in volume occupied by the vapour phase (also described by [30]). This consumption of CH_4 will cause a pressure drop until hydrate and fluid phases are in equilibrium again.

The reaction is initially limited by the small hydrate surface area, which is related to hydrate saturation. As more hydrate forms, the surface area for the reaction also increases. On the other hand, the driving force for the reaction is largest at the start, gradually decreasing when more hydrate forms. This combined effect results in a reaction rate that is decreasing again when the system is close to equilibrium.

Higher salinity and higher temperature result in lower hydrate saturations. The presence of salt results in a smaller driving force for the reaction. Moreover, the consumption of H_2O for hydrate formation increases the salt molality in the remaining aqueous phase, further restricting the conditions for additional hydrate formation. Higher temperature also reduces the ultimate hydrate saturation, but the reaction occurs at a faster rate and steady state is reached at an earlier stage. This is inherent to the kinetic nature of the reaction, which is characterized by the Arrhenius-type relation (3.17).

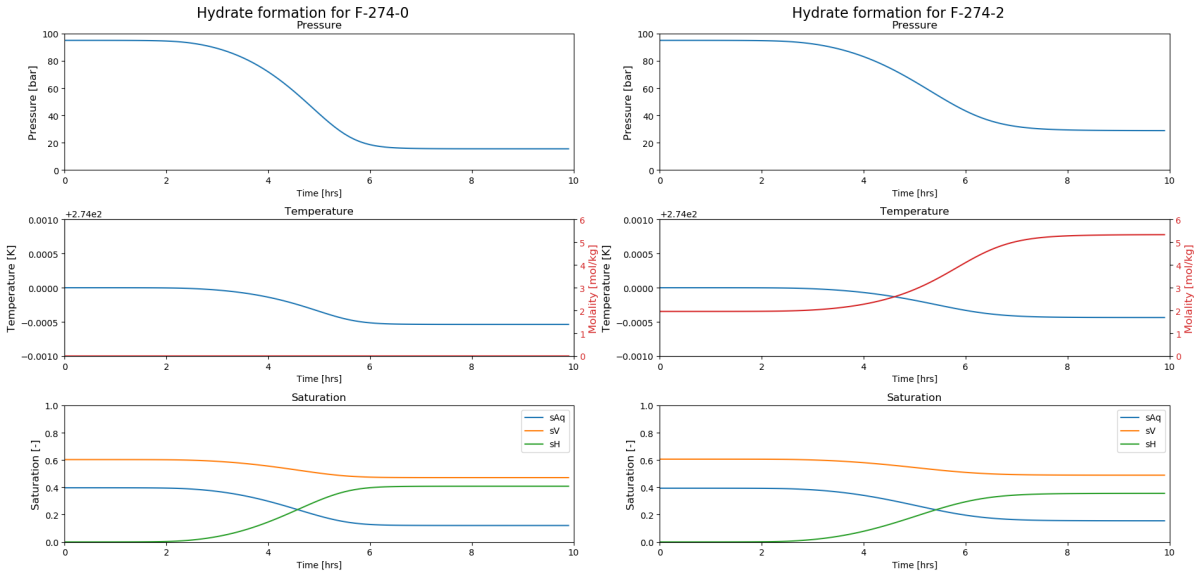

(a) Scenario F-274-0

(b) Scenario F-274-2

Figure 4.2: Results for 1-D formation scenario similar to Yin [30] at T=274 K

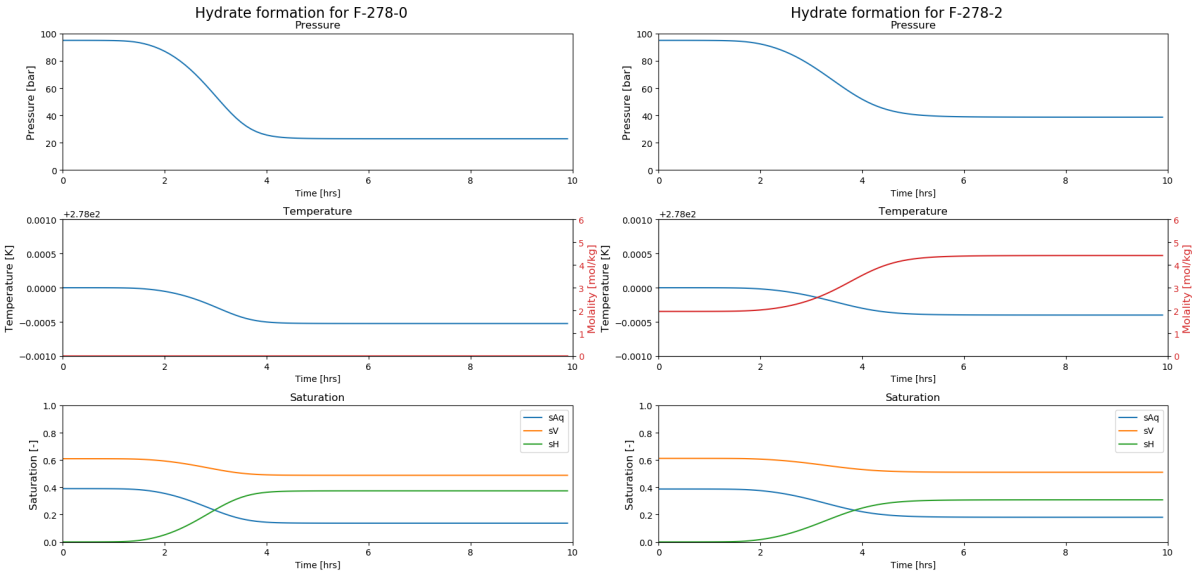

(a) Scenario F-274-0

(b) Scenario F-274-2

Figure 4.3: Results for 1-D formation scenario similar to Yin [30] at T=278 K

Table 4.3: Results for 1-D formation scenario similar to Yin [30]

Scenario	P_{end}	T_{end}	z_i			s_H
			CH_4	H_2O	$CH_4 \cdot nH_2O$	
F-274-0	15.55	274.0	0.035	0.690	0.276	0.408
F-274-2	28.88	274.0	0.057	0.676	0.202	0.356
F-278-0	22.91	278.0	0.048	0.721	0.231	0.374
F-278-2	38.72	278.0	0.072	0.716	0.156	0.309

4.2. Hydrate dissociation

Kowalsky [14] compared the use of kinetic and equilibrium reaction models in the simulation of hydrate behaviour in porous media. Here, we attempt to obtain results for a similar simulation for the depressurization scenario, with an extension to saline conditions. Results from Kowalsky [14] are shown in Figure 4.4.

Scenario description A hydrate-bearing reservoir, initially at equilibrium, is depressurized by withdrawing fluids through a producer. The hydrate will start to dissociate as soon as the pressure is lowered. The cylindrical reservoir from Kowalsky [14] is reduced to a 50-m 1-D reservoir with a producer at the left end (see Table 4.1). Simulation details are listed in Table 4.4.

The simulator used in Kowalsky [14] assumes that hydrate is stable above the supposed hydrate equilibrium pressure. No gas phase is present initially, pressure and temperature are above hydrate formation conditions and remain so until the pressure wave reaches this point in the reservoir, after which dissociation starts. However, this assumption is not valid when there is no sufficient supply of gas. In their simulation, no dissociation occurs and the pressure remains at initial pressure; in reality, either hydrates will form or dissociate in order to restore equilibrium, which will change pressure and composition.

If the system is not sufficiently close to equilibrium at the initialization of the simulation, rapid dissociation or formation will occur in order to restore equilibrium, which can significantly change the simulation results. In future simulations, it would be better to include the formation stage in the simulation, then let the system converge to equilibrium, and start the dissociation stage from that point.

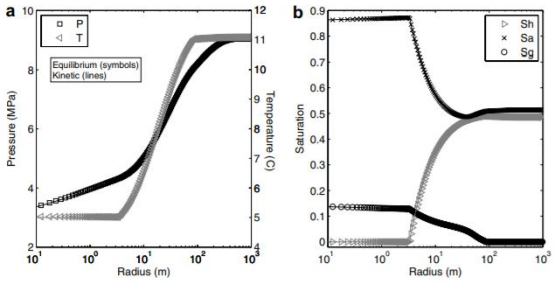

Figure 4.4: Results in Kowalsky [14] with a) pressure and temperature distribution and b) hydrate, aqueous and vapour saturation distribution after 30 days

Simulation results The simulation results for the dissociation scenarios are presented in Figure 4.5. It shows the state of the system four days after depressurization starts.

Under the conditions at the start of the simulation, the system will rapidly converge to the equilibrium pressure, as the rate of the reaction is high due to a large reaction surface area. The system is very sensitive to small changes in initial composition or deviations from the equilibrium pressure. Then, hydrate starts to dissociate when the production well is withdrawing fluids, depressurizing the system. The expanding gas that is being released from dissociating hydrates will push the aqueous phase away, possibly resulting in the dip in saturation of the aqueous phase in the region undergoing dissociation. Behind this region, the system is at equilibrium pressure. There is no communication between the regions to the left and right of the dissociation front, possibly because the pressure is maintained at the equilibrium pressure with the aid of the expanding gas released from dissociation.

With increasing salinity, the dissociation region extends along a larger length scale. This is related to the decreasing salinity of pore water upon fresh water release from the dissociation reaction. The driving force for dissociation then reduces, slowing down the reaction.

Table 4.4: Initial conditions for 1-D dissociation scenario similar to Kowalsky [14]

Scenario	$P_{initial}$	P_{well}	$T_{initial}$	z_i			Molality
				CH_4	H_2O	$CH_4 \cdot nH_2O$	
284-0	40.00	30.00	284.0	0.003	0.897	0.1	0.0
284-2	70.00	45.00	284.0	0.003	0.861	0.1	2.0

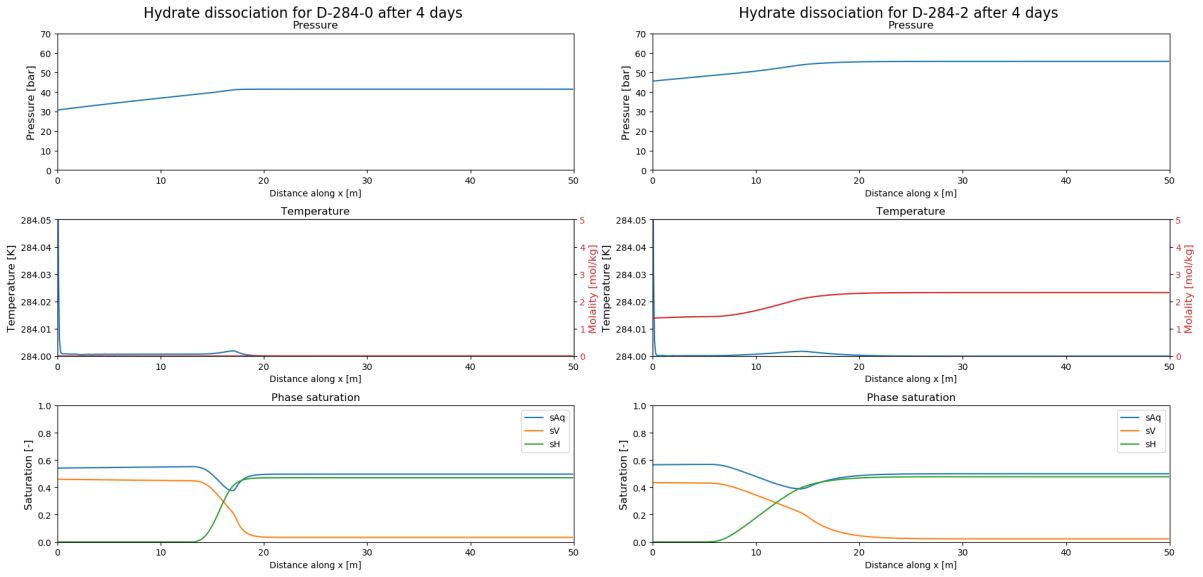

(a) Scenario D-284-0 after 10 days

(b) Scenario D-284-2 after 10 days

Figure 4.5: Results for 1-D dissociation scenario similar to Kowalsky [14] at T=284 K

5

Discussion

The aim of this study was to develop a simulation model that describes the formation and dissocation of methane hydrates under varying pressure, temperature and composition. The effect of water salinity on hydrate behaviour has been taken into account in thermodynamic models. This section will review the most important issues raised during the development of the model and discuss assumptions and limitations.

Review of the development of the model

Developing a flow-simulator for hydrate systems involves two major aspects: modelling of fluid flow through porous media, and modelling of thermodynamic behaviour of the hydrate-bearing system. As the framework for fluid-flow modelling in this work was taken from previous studies involving operator-based linearization [11, 29], the main focus of this work has been to extend this framework to include the thermodynamic behaviour of hydrate systems under kinetic conditions.

The assumption of a kinetic rate based on the difference in fugacity between current pressure and a presumed hydrate equilibrium pressure often proposed is not accurately describing the physics behind hydrate formation and dissociation. This does not capture the fact that hydrates will not be stable if there is no sufficient supply of gas. The fugacity relation from Van der Waals and Platteeuw [4, 28] provides a more accurate description of the stability of hydrates and the associated kinetic reaction. The operator-based linearization technique [29] simplifies the implementation of such complicated physics, since no analytical derivatives of state-dependent physics are required.

Moreover, advanced relative permeability models have been implemented based on experimental studies [3, 17]. The framework behind operator-based linearization offers the possibility to test and implement empirical models to better capture the flow dynamics of hydrate systems.

The implementation of the energy equation is necessary. Apart from the fact that hydrate formation and dissociation are strongly exothermic and endothermic processes, respetively [6], a simulator for methane hydrates under isothermal conditions is not validated considering Gibbs' phase rule. With three components (CH_4, H_2O and CH_4-hydrate), three phases (V, Aq and H), one kinetic reaction and temperature fixed, the system has no degrees of freedom and, as a result, will converge to a certain equilibrium pressure.

The current model is still very much a simplification of the actual pore-scale processes in hydrate systems. Comparison of results with literature [14, 30] shows similar behaviour and trends. However, further implementation of hydrate-related physics is required before it is meaningful to apply the model to experiments and validate through history matching and move to field-scale application of the simulator.

Review of assumptions and limitations

Assumptions made in the development of the model pose limitations to the accuracy of the results. Further development of the model might relax some assumptions. This section discusses the effect of the assumptions and their limitations to the current model.

Hydrate growth Many parameters in the model involve hydrate growth patterns, of which most notably permeability and reaction models. Permeability ultimately determines reservoir quality and the use of accurate models for hydrate growth is therefore crucial in hydrate modelling and the associated assessment of

reservoir potential. Moreover, reaction rates are assumed to be proportional to the surface area of the hydrate. However, the correlation for reaction surface area is derived from the assumption of hydrate being spherical particles in the voids of the sandy porous medium.

According to Almenningen [1], the assumption of pore-filling (or pore-coating) hydrate growth often used in models is too simplistic and hydrate growth occurs in a highly heterogeneous manner. A more accurate (pore-scale) description of hydrate growth and the effect of the nature of the porous medium is desirable in order to better describe the physics of hydrate systems on core- and field-scale.

Reaction constant Apart from the reaction constant taken as a rough estimate to compare results with literature, its value might also be evaluated as a function of other variables, optimized with history matching, similar to the surface area adjustment factor as suggested by Yin [30].

Fugacity of hydrate guest The statistical mechanical model by Van der Waals and Platteeuw [28] relates the fugacity of water in the hydrate to the fugacity of water in the aqueous phase (see Appendix B.2.2). Here, the fugacity of water in the hydrate phase is affected by the fugacity of the guest molecules occupying the hydrate cages. Under equilibrium assumptions, the fugacity of the guest molecule in hydrate is, by definition, equal to the fugacity of the guest molecule in the other phases. However, under kinetic conditions, a separate description of guest fugacity might be more accurate. The assumption of equal fugacity to other phases works (see Appendix B.2.2), but is a simplification that is not validated based on the statistical mechanical model.

Heat associated with hydrate reaction Hydrate formation is an exothermic process, and conversely dissociation is endothermic. Capturing the effect of heat exchange within hydrate systems upon both formation and dissociation is important, as temperature changes with hydrate formation or dissociation can result in the formation of secondary hydrates or ice upon dissociation and regained hydrate stability [6] and heat release upon hydrate formation might restrict further hydrate formation.

Range of applicability for models The thermodynamic and thermophysical models used in these simulations have often been developed for deeper-subsurface applications, where pressure and temperature are generally higher.

The thermodynamic behaviour of hydrate systems is a primary issue in modelling hydrates. The validity of thermodynamic models, describing phase partitioning and fugacity relations, is therefore crucial in obtaining accurate results. Temperatures close to freezing point of water ($< 5°C$) are at the edge of the range of consideration for Ziabaksh [32]. The use of the Peng-Robinson EoS [22] is valid for a vapour phase containing mostly methane, but becomes more problematic with the presence of polar components (e.g., H_2O). The Van der Waals and Platteeuw model for sI-type methane hydrate fugacity has proven to be accurate at the range of pressure and temperature of consideration for this work [4]. A graphical presentation of thermodynamic behaviour from the models used has been included in Appendix C.1.

The correlation for vapour viscosity by Lee [15] has been developed for slightly higher temperatures ($35 - 170°C$). The relation for water viscosity proposed by Mao [18] is applicable for temperatures larger than 273 K and from a pressure of 1 bar. Taking density from Spivey [27] and Peng-Robinson [22] is valid for the purpose of this study. A graphical presentation of viscosity and density models can be found in Appendix C.2.

When the model is to be extended to conditions below freezing point, which is necessary when permafrost is considered, it will be useful to re-evaluate the selection of thermodynamic and thermophysical models.

6

Conclusions and recommendations

6.1. Conclusions

The aim of this work was to develop a predictive simulation model for gas hydrates formation and dissociation, based on core-scale experimental results. The existing DARTS-framework has been extended to include a kinetic description of the hydrate formation and dissociation reaction. Ultimately, a non-isothermal model has been tested for 1-D formation and dissociation cases. Comparison of results with literature shows similar behaviour and trends. The effect of water salinity has also been captured by the model, which has to be validated with experimental results. However, further development of the model is required in order to match measured data.

6.2. Recommendations and future work

Equilibrium description A kinetic model is recommended in the description of short-term processes to capture the complexity of gas hydrate formation and dissociation [14]. For longer-term processes, treating the formation and dissociation of hydrates as an equilibrium reaction is appropriate [30]. Modelling gas hydrates under equilibrium conditions might be more computationally efficient, as methane hydrate does not have to be tracked as a separate component, reducing the number of equations to be solved.

Mixed hydrates Incorporating the inclusion of different guest molecules by the hydrate, as well as different hydrate cage types, ultimately offers the possibility to investigate and assess the feasibilty of carbon sequestration and methane production and develop strategies for field-scale exploitation of hydrate reservoirs. Implementation of equilibrium reaction models for mixed hydrates is relatively straightforward. However, a kinetic reaction model requires more thorough understanding of the governing physics on a molecular scale.

Capillary, diffusive and gravity effects An accurate description of pore-scale processes must include capillary forces and diffusive fluxes. Capillary forces will be even more pronounced when the presence of hydrates reduces the available pore space and the size of the pores available for flow. Diffusion plays a significant role in hydrate-filled pores as advective flow of fluids is limited. Moreover, there might be large gradients in salt concentrations as a result of fresh water release or consumption upon hydrate formation or dissociation, which is important to capture given the sensibility of hydrate stability to pore water salinity. The effect of gravity can have a pronounced effect on the behaviour of the hydrate system as a whole, redistributing vapour and aqueous phases as methane and water are being consumed or released in the hydrate reaction.

Development, implementation and validation of empirical models Simulation of experiments provides a tool for testing, improving and optimizing models for hydrate behaviour through history matching with experimental data. With DARTS, complex correlations (e.g., a relation for relative permeability for a wide range of hydrate saturations, as suggested by Mahabadi [17]) can be implemented and tested with relative ease.

Coupling with geomechanical model A predictive model for fluid flow in hydrate systems combined with a geomechanical model can provide valuable insight into the mechanical behaviour of hydrate accumulations and their response to hydrate formation and dissociation.

Bibliography

[1] S. Almenningen and G. Ersland. Water permeability measurements on hydrate-saturated sandstone cores with immobile gas. August 2017.

[2] S. Almenningen, P. Fotland, M. Fernø, and G. Ersland. An experimental investigation of gas-production rates during depressurization of sedimentary methane hydrates. *SPE Journal*, 190811, September 2018.

[3] S. Almenningen, J. Gauteplass, L. Hauge, T. Barth, M. Fernø, and G. Ersland. Measurements of CH_4 and CO_2 relative permeability in hydrate-bearing sandstone. *Journal of Petroleum Science and Engineering*, 177:880–888, March 2019.

[4] A.L. Ballard. *A non-ideal hydrate solid solution model for a multi-phase equilibria program.* PhD thesis, Colorado School of Mines, 2002.

[5] C. Berndt, S. Bünz, T. Clayton, J. Mienert, and M. Saunders. Seismic character of bottom simulating reflectors: examples from the mid-norwegian margin. *Marine and Petroleum Geology*, 21:723–733, February 2004.

[6] K.A. Birkedal, C.M. Freeman, G.J. Moridis, and A. Graue. Numerical predictions of experimentally observed methane hydrate dissociation and reformation in sandstone. *Energy Fuels*, 28:5573–5586, August 2014.

[7] C. Ecker, J. Dvorkin, and A. Nur. Sediments with gas hydrates: Internal structure from seismic avo. *Geophysics*, 63(5):1496–1823, September 1998.

[8] G. Ersland, J. Husebø, A. Graue, B.A. Baldwin, J. Howard, and J. Stevens. Measuring gas hydrate formation and exchange with CO_2 in bentheim sandstone using mri tomography. *Chemical Engineering Journal*, 158:25–31, December 2008.

[9] S.E. Harrison. Natural gas hydrates. `http://large.stanford.edu/courses/2010/ph240/harrison1/`, October 2010. Accessed: 2019-11-17.

[10] A. Iranshahr, D.V. Voskov, and H.A. Tchelepi. Generalized negative-flash method for multiphase multicomponent systems. *Fluid Phase Equilibria*, 299:272–284, September 2010.

[11] K. Kala and D.V. Voskov. Element balance formulation in reactive compositional flow and transport with parameterization technique. *Computational Geosciences*, June 2019.

[12] H.C. Kim, P.R. Bishnoi, R.A. Heidemann, and S.S.H. Rizvi. Kinetics of methane hydrate decomposition. *Chemical Engineering Science*, 42(7):1645–1653, 1987.

[13] J. Klein. Methane has never looked so beautiful. *The New York Times*, 8 March 2016. Available: `https://www.nytimes.com/2016/03/08/science/methane-has-never-looked-so-beautiful.html`. Accessed: 2019-17-11.

[14] M.B. Kowalsky and G.J. Moridis. Comparison of kinetic and equilibrium reaction models in simulating gas hydrate behavior in porous media. *Energy Conversion and Management*, 48:1850–1863, February 2007.

[15] A.L. Lee and M.H. Gonzalez. The viscosity of natural gases. *Journal of Petroleum Technology*, August 1966.

[16] T.M. Letcher. *Future energy: Improved, sustainable and clean options for our planet.* Elsevier, London, 2nd edition, 2013.

[17] N. Mahabadi, S. Dai, Y. Seol, T.S. Yun, and J. Jang. The water retention curve and relative permeability for gas production from hydrate-bearing sediments: pore-network model simulation. *Geochemistry, Geophysics, Geosystems*, 17:3099–3110, August 2016.

[18] S. Mao and Z. Duan. The viscosity of aqueous alkali-chloride solutions up to 623k, 1000 bar, and high ionic strength. *International Journal of Thermophysics*, 30:1510–1523, September 2009.

[19] L. Marini. *Geological Sequestration of Carbon Dioxide: Thermodynamics, Kinetics, and Reaction Path Modeling*. Elsevier, Amsterdam, 1st edition, 2007.

[20] G.J. Moridis. *User's manual for the hydrate v1.5 option of TOUGH+ v1.5: A code for the simulation of system behavior in hydrate-bearing geologic media*. Earth Sciences Division, Lawrence Berkeley National Laboratory, Berkeley, CA 94720, August 2014.

[21] K.S. Pedersen and P.L. Christensen. *Phase Behavior of Petroleum Reservoir Fluids*. CRC Press, Boca Raton, 1st edition, December 2007.

[22] D. Peng and D.B. Robinson. A new two-constant equation of state. *Ind. Eng. Chem.*, 15(1):59–64, September 1976.

[23] A. Péneloux, E. Rauzy, and R. Fréze. A consistent correction for redlich-kwong-soave volumes. *Fluid Phase Equilibria*, 8:7–23, September 1982.

[24] K. Qorbani, B. Kvamme, and R. Olsen. Sensitivity analysis of CO_2 injection within saline aquifers for storage purposes in the form of hydrate using a reactive transport simulator. *Journal of Chemical and Engineering Data*, 61:4148–4156, September 2016.

[25] C.D. Ruppel and J.D. Kessler. The interaction of climate change and methane hydrates. *Review of Geophysics*, 55:126–168, February 2017.

[26] E.D. Sloan Jr. and C. Koh. *Clathrate Hydrates of Natural Gases*. CRC Press, Boca Raton, 2007.

[27] J.P. Spivey, W.D. McCain Jr., and R. North. Estimating density, formation volume factor, compressibility, methane solubility, and viscosity for oilfield brines at temperatures from 0 to 275Celsius, pressures to 200 mpa, and salinities to 5.7 mole/kg. *Journal of Canadian Petroleum Technology*, 43(7):52–61, July 2004.

[28] J. Van der Waals and J. Platteeuw. Validity of clapeyron's equation for phase equilibria involving clathrates. *Nature*, 183(462), February 1959.

[29] D.V. Voskov and M. Khait. Operator-based linearization approach for modeling of multiphase multi-component flow in porous media. *Journal of Computational Physics*, 337:275–288, August 2017.

[30] Z. Yin, G. Moridis, H.K. Tan, and P. Linga. Numerical analysis of experimental studies of methane hydrate formation in a sandy porous medium. *Applied Energy*, 220:681–704, April 2018.

[31] C.M.R. Yonkofski, J.A. Horner, and M.D. White. Experimental and numerical investigation of hydrate-guest molecule exchange kinetics. *Journal of Natural Gas Science and Engineering*, 35:1480–1489, April 2016.

[32] Z. Ziabaksh-Ganji and H. Kooi. An equation of state for thermodynamic equilibrium of gas mixtures and brines to allow simulation of the effects of impuritiets in subsurface CO_2 storage. *International Journal of Greenhouse Gas Control*, 11S:S21–S34, August 2012.

A

Listing of input units in DARTS

Table A.1: Input units for mass conservation equation used in DARTS (2.12)

Operator	Parameter	Symbol	Unit
Accumulation			
$a(\xi)$			
	Cell volume	V	m^3
	Porosity	ϕ	-
$\alpha(\omega)$			
	Phase saturation	s_j	-
	Phase molar density	ρ_{mj}	mol m^{-3}
	Phase composition	x_{ij}	-
Flux			
$b(\xi,\omega)$			
	Time step	Δt	day
	Geometric part of transmissibility	Γ^l	mD.m
	Pressure	P	bar
$\beta(\omega)$			
	Phase composition	x_{ij}	-
	Phase molar density	ρ_{mj}	mol m^{-3}
	Phase relative permeability	k_{rj}	-
	Phase viscosity	μ_j	cP
Source			
$c(\xi)$			
	Time step	Δt	day
	Volume	V	m^3
$\gamma(\omega)$			
	Stoichiometric constant	v_{ik}	-
	Reaction rate	r_k	mol m^{-3} day^{-1}
$d(\xi,\omega,\mathbf{u})$			
	Time step	Δt	day
	Injection rate	q_j	m^3 day^{-1}
$\theta(\omega)$			
	Phase composition	x_{ij}	-
	Phase molar density	ρ_{mj}	mol m^{-3}

It must be noted here that, in order to have consistent units of [mol] for each term, the flux term ($b(\xi,\omega)$) in both the mass and energy residuals is multiplied by a factor of $8.5267 \cdot 10^{-3}$.

Table A.2: Input units for energy conservation equation used in DARTS (2.14)

Operator	Parameter	Symbol	Unit
Accumulation			
$a_\theta(\xi)$			
	Cell volume	V	m^3
	Porosity	ϕ	-
$\alpha_\theta(\omega)$			
	Phase saturation	s_j	-
	Phase molar density	ρ_{mj}	mol m^{-3}
	Phase specific internal energy	U_j	kJ mol^{-1}
	Rock volumetric internal energy	U_r	kJ m^{-3}
Flux			
$b_\theta(\xi,\omega)$			
	Time step	Δt	day
	Geometric part of advective transmissibility	Γ^l	mD.m
	Pressure	P	bar
$\beta_\theta(\omega)$			
	Phase specific enthalpy	h_j	kJ mol^{-1}
	Phase molar density	ρ_{mj}	mol m^{-3}
	Phase relative permeability	k_{rj}	-
	Phase viscosity	μ_j	cP
$c_\theta(\xi,\omega)$			
	Time step	Δt	day
	Geometric part of conductive transmissibility	Γ_c^l	m
	Temperature	T	K
$\gamma_\theta(\omega)$			
	Composite thermal conductivity	$\overline{\kappa}$	kJ m^{-1} K^{-1} day^{-1}
Source			
$d_\theta(\xi,\omega,\mathbf{u})$			
	Time step	Δt	day
	Injection rate	q_j	m^3 day^{-1}
$\theta_\theta(\omega)$			
	Phase specific enthalpy	h_j	kJ mol^{-1}
	Phase molar density	ρ_{mj}	mol m^{-3}

Table A.3: Input units for geometric transmissibility

	Parameter	Symbol	Unit
Γ^l	Surface area of boundary l	A_l	m^2
	Absolute permeability in cell m	k_m	mD
	Distance between centre of cell m and boundary l	D_m	m
Γ_c^l	Surface area of boundary l	A_l	m^2
	Distance between centre of cell m and boundary l	D_m	m

B

Listing of model parameters

B.1. Component properties

For the components considered in the model, some properties frequently used in correlations are given in Table B.1.

Table B.1: Component properties

	H_2O	CH_4	CO_2	N_2	H_2S	NaCl
T_c	647.14	190.58	304.10	126.20	373.53	-
P_c	220.50	46.04	73.75	34.00	89.63	-
M_w	18.015	16.043	44.01	28.013	34.076	58.44
ω	0.328	0.012	0.239	0.0377	0.0942	-
Z_c		0.286	0.274	0.289		-

The binary interaction coefficients used in Peng-Robinson EoS are tabulated in B.2.

Table B.2: Binary interaction parameters for Peng Robinson EoS

	H_2O	CH_4	CO_2	N_2	H_2S
H_2O	0	0.47893	0.19014	0.32547	0.105
CH_4		0	0.100	0.0311	0.0503
CO_2			0	-0.017	0.0974
N_2				0	0.1767
H_2S					0

B.2. Fugacity relations and K-values

B.2.1. Ideal K-values

Vapour and aqueous phases Following Ballard [4], the ideal distribution coefficient between vapour V and aqueous Aq can be found by taking the standard Raoult's law as:

$$x_{iV}\phi_{iV}P = x_{iAq}\gamma_{iAq}P_i^{sat}\exp\left[\int_{P_i^{sat}}^{P}\frac{v}{RT}\,dP\right] \tag{B.1}$$

and assume that 1) component i in the aqueous phase is very dilute and therefore, γ_{iAq} can be approximated by the infinite dilution activity coefficient γ_{iAq}^{∞}, 2) the fugacity coefficient ϕ_{iV} of component i equals unity and 3) the exponential term, referred to as the Poynting correction factor, equals unity. This reduces the modified Raoult's law to:

$$K_i = \frac{x_{iV}}{x_{iAq}} = \frac{P_i^{sat}}{P}\gamma_{iAq}^{\infty} \tag{B.2}$$

Saturation pressure can be described by:

$$P_i^{sat} = P_{c_i} \exp[a_1 + \omega_i a_2] \tag{B.3}$$

Coefficients for saturation pressure for hydrocarbons (B.3) are calculated as:

$$a_i = a_{i1} + a_{i2}\frac{T_{c_i}}{T} + a_{i3}\ln\frac{T}{T_{c_i}} + a_{i4}\frac{T^6}{T_{c_i}^6} \tag{B.4}$$

where the coefficients a_{ij} are listed in Table B.3.

Table B.3: Coefficients for (B.4)

i	a_{i1}	a_{i2}	a_{i3}	a_{i4}
1	5.927140	-6.096480	-1.288620	0.169347
2	15.25180	-15.68750	-13.47210	0.43577

For water, the standard Antoine equation is used for the saturation pressure:

$$P_i^{sat} = \exp\left[a_{1_i} - \frac{a_{2_i}}{T + a_{3_i}}\right] \tag{B.5}$$

for which coefficients a_1, a_2 and a_3 can be found in Table B.4.

The infinite dilution activity coefficient for hydrocarbons (n-paraffins) is given by:

$$\gamma_{iAq}^{\infty} = \exp\left[a_1 + a_2 N_i + \frac{a_3}{N_i}\right] \tag{B.6}$$

where N_i is the total number of carbon atoms in molecule i. The infinite dilution activity coefficient for water is assumed to be equal to one. Coefficients for (B.6) are tabulated in Table B.4.

Table B.4: Coefficients for (B.6)

	a_1	a_2	a_3
(B.5)	12.048399	4030.18245	-38.15
(B.6)	0.688	0.642	0

B.2.2. Updated fugacity and K-values

Vapour and liquid hydrocarbon phases The expression for Peng-Robinson [22] reads:

$$P = \frac{RT}{v-b} - \frac{a(T)}{v(v+b)+b(v-b)} \tag{B.7}$$

Equation (B.7) can be rewritten as

$$Z^3 - (1-B)Z^2 + (A - 3B^2 - 2B)Z - (AB - B^2 - B^3) = 0 \tag{B.8}$$

where A and B are coefficients described by:

$$A = \frac{aP}{R^2T^2} \tag{B.9}$$

$$B = \frac{bP}{RT} \tag{B.10}$$

Here, a and b are the intermolecular attraction parameter and a constant related to the size of the molecules, respectively [22]. These coefficients are related to the critical properties. At the critical point, we have:

$$a(T_c) = 0.457235\frac{R^2T_c^2}{P_c} \tag{B.11}$$

$$b(T_c) = 0.077795\frac{RT_c}{P_c} \tag{B.12}$$

At temperatures other than critical, $b(T)$ is equal to $b(T_c)$, but a reads:

$$a(T) = a(T_c) \cdot \alpha(T_r, \omega) \tag{B.13}$$

Here, α is a parameter related to the vapour pressure of a component and can take on various forms. Peng-Robinson derived the following relation between α, T_r and ω:

$$\alpha^{1/2} = 1 + \kappa\left(1 - T_r^{1/2}\right) \tag{B.14}$$

where

$$\kappa = 0.37464 + 1.54226\omega - 0.26992\omega^2 \tag{B.15}$$

The coefficients described here are for pure components. The Peng-Robinson equation of state can be extended to mixtures by using the mixing rules:

$$a = \sum_i \sum_j x_i x_j a_{ij} \tag{B.16}$$

$$b = \sum_i x_i b_i \tag{B.17}$$

where x_i and x_j denote the vapour or liquid hydrocarbon mole fractions and

$$a_{ij} = (1 - \delta_{ij}) a_i^{1/2} a_j^{1/2} \tag{B.18}$$

Here, δ_{ij} denotes an empirically determined binary interaction coefficients characterizing the binary formed by component i and component j and $\delta_{ij} = \delta_{ji}$. Values for δ_{ij} are given in Table B.2.

The compressibility factor Z is described by the real gas law:

$$Z = \frac{PV_m}{RT} \tag{B.19}$$

Equation (B.8) has three roots for Z, of which either one or three are real depending upon the number of phases in the system. In the two-phase region, the largest root is for the compressibility factor of the vapour while the smallest positive root corresponds to that of the liquid. In case equation (B.8) has only one real root, the system is in the supercritical region and contains only a single hydrocarbon phase. Once the compressibility factor of a phase is found, the fugacity coefficient of a phase can be found through the relation:

$$\ln \phi_{ij} = \frac{b_i}{b}(Z_j - 1) - \ln(Z_j - B) - \frac{A}{2\sqrt{2}B}\left(\frac{2\sum_i x_i a_{ij}}{a} - \frac{b_i}{b}\right) \ln\left(\frac{Z_j + 2.414B}{Z_j - 0.414B}\right) \tag{B.20}$$

Density correction

As liquid density predictions from the Peng-Robinson equation of state are not very accurate, a correction is used to improve the accuracy of density predictions of the Peng-Robinson EoS. The volume shift parameter developed by Peneloux [23] modifies the original volume of the equation of state by the following equations:

$$V_{Pen} = V_{PR} - c \tag{B.21}$$

$$b_{Pen} = b_{EoS} - c \tag{B.22}$$

where Pen and PR denote Peneloux and original Peng-Robinson values and c is the volume shift parameter. It is a parameter influencing molar volumes and phase densities without influencing the phase equilibrium [21]. For components lighter than heptane, the component-specific volume shift parameter of the PR equations of state is defined by:

$$c_i = \frac{0.50033 R T_c}{P_c}\left(0.25969 - Z_{RA}\right) \tag{B.23}$$

where Z_{RA} is the Rackett compressibility factor which is expressed as a function of acentric factor as:

$$Z_{RA} = 0.29056 - 0.08775\omega \tag{B.24}$$

For mixtures, volume shift parameter c reads:

$$c = \sum_i x_i c_i \tag{B.25}$$

The Peneloux correction not only corrects liquid-phase densities but also the vapour-densities. Because the vapour-phase molar volumes are high, the volume correction, however, has only a minor influence on the gas volumes but a significant influence on the liquid volumes (Pedersen, 2007).

Aqueous phase For the aqueous phase, the chemical potential is written in terms of activity rather than fugacity, following the procedure described by Ziabaksh [32]. Salt is assumed to be only present in the aqueous phase, but its effect on the activity of other components is accounted for in terms of molality. Salt molality is defined as the amount of moles of solute per kg of solvent (H_2O) and is related to mole fraction according to:

$$m = \frac{1000 \cdot x_{\mathrm{NaCl},Aq}}{M_{w,\mathrm{H_2O}} \cdot x_{\mathrm{H_2O},Aq}} = 55.509 \frac{x_{\mathrm{NaCl},Aq}}{x_{\mathrm{H_2O},Aq}} \tag{B.26}$$

where $x_{\mathrm{NaCl},Aq}$ is equal to the mole fraction of salt in the aqueous phase and $x^*_{\mathrm{H_2O},Aq}$ denotes the re-normalized water mole fraction of the aqueous phase (as mole fractions are normalized for salt at this point), which can be found through re-normalizing the aqueous phase mole fractions as:

$$x^*_{\mathrm{H_2O},Aq} = z_{\mathrm{H_2O}_{(Aq)}} = \nu_{\mathrm{H_2O}} \cdot x_{\mathrm{H_2O},Aq} \cdot (1 - z_{\mathrm{NaCl}_{(Aq)}}) \tag{B.27}$$

For all other components, except water, the partitioning between aqueous and non-aqueous (vapour) phase is described by:

$$\left(P \phi_i y_i\right)_{NAq} = \left(k_H \gamma_i x_i\right)_{Aq} \tag{B.28}$$

where ϕ_i denotes the fugacity coefficient of the non-aqueous phase phase (from Peng-Robinson EoS), k_H is Henry's constant and γ_i is the activity coefficient of component i. Henry's constant can be quantified for all dissolved gases as:

$$\ln k_H = (1-\eta) \ln f^0_{\mathrm{H_2O}} + \eta \ln\left(\frac{RT}{M_{w,\mathrm{H_2O}}} \rho^0_{\mathrm{H_2O}}\right) + 2\rho^0_{\mathrm{H_2O}} \Delta B \tag{B.29}$$

where

$$\Delta B = \tau + \Gamma P + \beta \sqrt{\frac{10^3}{T}} \tag{B.30}$$

Here, τ [$\mathrm{cm^3\ g^{-1}}$], β [$\mathrm{cm^3\ K^{0.5}\ g^{-1}}$] and Γ [$\mathrm{bar^{-1}}$] denote adjustable parameters for each dissolved species, tabulated in Table B.5. For the calculation of properties of pure water, Ziabaksh [32] follows the correlation described in (B.31)-(B.34) below:

$$V = \frac{V^0 - V^0 P}{B + A_1 P + A_2 P^2} \tag{B.31}$$

where

$$V^0 = \frac{1 + 18.159725 \cdot 10^{-3}\theta}{0.9998396 + 18.224944 \cdot 10^{-3}\theta - 7.922210 \cdot 10^{-6}\theta^2 - 55.44846 \cdot 10^{-9}\theta^3 + 149.7562 \cdot 10^{-12}\theta^4 - 393.2952 \cdot 10^{-15}\theta^5} \tag{B.32}$$

with

$$\begin{aligned} B &= 19654.320 + 147.037\theta - 2.21554\theta^2 + 1.0478 \cdot 10^{-2}\theta^3 - 2.2789 \cdot 10^{-5}\theta^4 \\ A_1 &= 3.2891 - 2.3910 \cdot 10^{-3}\theta + 2.8446 \cdot 10^{-4}\theta^2 - 2.8200 \cdot 10^{-6}\theta^3 + 8.477 \cdot 10^{-9}\theta^4 \\ A_2 &= 6.245 \cdot 10^{-5} - 3.913 \cdot 10^{-6}\theta - 3.499 \cdot 10^{-8}\theta^2 + 7.942 \cdot 10^{-10}\theta^3 - 3.299 \cdot 10^{-12}\theta^4 \end{aligned}$$

Here, θ is temperature in Celsius and $V = 1/\rho^0_{\mathrm{H_2O}}$ is the reciprocal of the density of pure water [$\mathrm{cm^{3\ -1}}$]. The fugacity of pure water is described by:

$$f^0_{\mathrm{H_2O}} = P_s \exp\left[\frac{(P - P_s) V M_w}{RT}\right] \tag{B.33}$$

where P_s can be calculated by:

$$\begin{aligned} \ln\left(\frac{P_s}{P_c}\right) = \frac{T_c}{T}\Bigg[&-7.85951783\frac{T}{T_c} + 1.84408259\left(\frac{T}{T_c}\right)^{1.5} - 11.7866497\left(\frac{T}{T_c}\right)^{3} + 22.6807411\left(\frac{T}{T_c}\right)^{3.5} \\ &- 15.9618719\left(\frac{T}{T_c}\right)^{4} + 1.80122502\left(\frac{T}{T_c}\right)^{7.5}\Bigg] \end{aligned} \tag{B.34}$$

The activity coefficient for non-water components can be calculated according to:

$$\ln \gamma_i = \sum_C 2 m_C \lambda_{i-C} + \sum_A 2 m_A \lambda_{i-A} + \sum_C \sum_A m_A m_C \xi_{i-C-A} \tag{B.35}$$

Table B.5: Coefficients for (B.29) and (B.30)

	η	τ	β	Γ
CH_4	-0.092248	-5.779280	7.262730	0
CO_2	-0.114535	-5.279063	6.187967	0
N_2	-0.008194	-5.175337	6.906469	0
H_2S	0.77357854	0.27049433	0.27543436	0
SO_2	0.198907	-1.552047	2.242564	-0.009847

where m_C and m_A denote cations and anions molality, respectively, and coefficients λ_{i-C} and ξ_{i-C-A} are described by:

$$Par(T,P) = c_1 + c_2 T + \frac{c_3}{T} + c_4 P + \frac{c_5}{P} + c_6 \frac{P}{T} + c_7 \frac{T}{P^2} + \frac{c_8 P}{630 - T} + c_9 T \ln P + c_{10} \frac{P}{T^2} \tag{B.36}$$

Parameter λ_{i-A} is assumed to be zero and for the parameters we assume $\lambda_{i-C} = \lambda_{i-Na}$ and $\xi_{i-C-A} = \xi_{i-Na-Cl}$. The coefficients for (B.36) are listed in Tables B.6 and B.7.

Table B.6: Coefficients for (B.36) for λ_{i-Na}

λ_{i-Na} i	CH_4	CO_2	N_2	H_2S	SO_2
c_1	$-5.7066455\cdot10^{-1}$	-0.0652869	-2.0939363	1.03658689	$-5.0961510\cdot10^{-2}$
c_2	$7.2997588\cdot10^{-4}$	$1.6790636\cdot10^{-4}$	$3.1445269\cdot10^{-3}$	$-1.1784797\cdot10^{-3}$	$2.8865149\cdot10^{-4}$
c_3	$1.5176903\cdot10^{2}$	40.838951	$3.9139160\cdot10^{2}$	$-1.7754826\cdot10^{2}$	0
c_4	$3.1927112\cdot10^{-5}$	0	$-2.9973977\cdot10^{-7}$	$-4.5313285\cdot10^{-4}$	0
c_5	0	0	0	0	$1.1145002\cdot10^{-2}$
c_6	$-1.6426510\cdot10^{-5}$	$-3.9266518\cdot10^{-2}$	$-1.5918098\cdot10^{-5}$	0	0
c_7	0	0	0	0	$-2.4878170\cdot10^{-5}$
c_8	0	$2.1157167\cdot10^{-2}$	0	0	0
c_9	0	$6.5486487\cdot10^{-6}$	0	0	0
c_{10}	0	0	0	$0.47751650\cdot10^{2}$	0

Table B.7: Coefficients for (B.36) for $\xi_{i-Na-Cl}$

$\xi_{i-Na-Cl}$ i	CH_4	CO_2	N_2	H_2S	SO_2
c_1	$-2.9990084\cdot10^{-3}$	$-1.144624\cdot10^{-2}$	$-6.3981858\cdot10^{-3}$	-0.010274152	$-7.1462699\cdot10^{-3}$
c_2	0	$2.8274958\cdot10^{-5}$	0	0	0
c_3	0	0	0	0	0
c_4	0	0	0	0	0
c_5	0	0	0	0	0
c_6	0	$1.3980876\cdot10^{-2}$	0	0	0
c_7	0	0	0	0	0
c_8	0	$-1.4349005\cdot10^{-2}$	0	0	0
c_9	0	0	0	0	0
c_{10}	0	0	0	0	0

For water, the partitioning between aqueous and non-aqueous (vapour or liquid) phases is described by [32]:

$$H_2O_{(l)} \rightleftharpoons H_2O_{(g)}$$

$$K^*_{H_2O} = \frac{f_{H_2O_{(g)}}}{a_{H_2O_{(l)}}} \tag{B.37}$$

Here, $K^*_{H_2O}$ is the "true equilibrium constant", which is a function of temperature and pressure as given by:

$$K^*_{H_2O} = K^0_{H_2O} \exp\left[\frac{(P - P_0) V_{H_2O}}{RT}\right] \tag{B.38}$$

Here, V_{H_2O} is the average partial molar volume over pressure interval from P to P_0, which is equal to 18.1. The reference pressure P_0 is assumed to be 1 bar. The equilibrium constant at reference pressure P_0 is obtained from:

$$\log\left(K^0_{H_2O}\right) = -2.209 + 3.097 \cdot 10^{-2} T - 1.098 \cdot 10^{-4} T^2 + 2.048 \cdot 10^{-7} T^3 \tag{B.39}$$

with T in °C.

Combining the left-hand side of (B.28), (B.37) and (B.38) gives a relation for the actual partitioning K-value between vapour and aqueous phases. At the range of consideration for pressure and temperature, the solubility of gases in water is low, and the activity of the water component can be approximated by its mole fraction in the aqueous phase, which yields:

$$K_{H_2O} = \frac{y_{H_2O}}{x_{H_2O}} = \frac{K^*_{H_2O}}{\phi_{H_2O,NAq} P} \tag{B.40}$$

From these relations, fugacity coefficients for the aqueous phase can be extracted by rewriting K-values as ratio of fugacity coefficients as described by (3.7). For all non-water components, the fugacity coefficient for the aqueous phase reads:

$$\phi_{iAq} = k_H \gamma_i / P \tag{B.41}$$

For water, the fugacity coefficient for the aqueous phase can be obtained by rewriting (B.40):

$$\phi_{H_2O,Aq} = K^*_{H_2O} / P \tag{B.42}$$

Hydrate phase Fugacity in the sI-type hydrate phase is determined through the method of Van der Waals and Platteeuw [28]. They used statistical thermodynamics to derive several thermodynamic properties of hydrates. Following this method in Ballard [4], fugacity of water in the hydrate phase is expressed by

$$f_{w,H} = f_{w,Aq} \exp\left[\frac{\Delta\mu_{w,H} - \Delta\mu_{w,Aq}}{RT}\right] \tag{B.43}$$

Here, the fugacity is related to the chemical potential of water in the hydrate phase to that in the aqueous phase. This is done by considering the energy change associated with forming a hydrate and an aqueous phase from an empty hydrate lattice at given volume, pressure and temperature (denoted by $g_{w,\beta}$).

For the aqueous phase, the change in energy is given by:

$$\frac{\Delta\mu_{w,Aq}}{RT} = \frac{\mu_{w,Aq} - g_{w,\beta}}{RT} \tag{B.44}$$

which is the difference between chemical potential of water in the aqueous phase and that in the empty hydrate. According to the classical expression:

$$\frac{\mu_{w,Aq}}{RT} = \frac{g_{w_0,Aq}}{RT_0} - \int_{T_0}^{T} \frac{h_{w,Aq}}{RT^2}\, dT + \int_{P_0}^{P} \frac{v_{w,Aq}}{RT}\, dP + \ln a_{w,Aq} \tag{B.45a}$$

$$\frac{g_{w,\beta}}{RT} = \frac{g_{w_0,\beta}}{RT_0} - \int_{T_0}^{T} \frac{h_{w,\beta}}{RT^2}\, dT + \int_{P_0}^{P} \frac{v_{w,\beta}}{RT}\, dP \tag{B.45b}$$

where $g_{w,j}$, $h_{w,j}$ and $v_{w,j}$ are the molar Gibbs energy, enthalpy and volume of water in pure liquid water or in the empty hydrate lattice, and the subscript 0 denotes reference conditions of 298.15 K and 1 bar. At the range of consideration for pressure and temperature, the solubility of gases in water is low, and the activity of the water component in the aqueous phase can be approximated by its mole fraction in the aqueous phase (see fugacity of aqueous phase). Following the relations used in Ballard (2002), this gives for the aqueous phase:

$$h_{w,Aq} = h_{w0} + \int_{T_0}^{T} c_{P_w}\, dT \tag{B.46a}$$

$$v_{w,Aq} = \sum_{i=0}^{3} \left(a_{1i} + a_{2i} P + a_{3i} P^2 + a_{4i} P^3\right) T^i \tag{B.46b}$$

where heat capacity at reference pressure is given by

$$c_{P_w} = a_0 + a_1 T + a_2 T^2 + a_3 T^3 \tag{B.47}$$

Table B.8: Parameters used in (B.45)-(B.46)

$g_{w_0,Aq}$	$h_{w_0 0}$	a_0/R	a_1/R	a_2/R	a_3/R
-237129	-285830	8.712	$0.125\cdot10^{-2}$	$-0.018\cdot10^{-5}$	$0\cdot10^{-9}$

Table B.9: Coefficients used in (B.46b)

i	0	1	2	3
a_{1i}	31.1251	$-1.41154\cdot10^{-1}$	$3.10034\cdot10^{-4}$	$-2.48318\cdot10^{-7}$
a_{2i}	$-2.46176\cdot10^{-2}$	$2.15663\cdot10^{-4}$	$-6.48160\cdot10^{-7}$	$6.47521\cdot10^{-10}$
a_{3i}	$8.69425\cdot10^{-6}$	$-7.96939\cdot10^{-8}$	$2.45391\cdot10^{-10}$	$-2.51773\cdot10^{-13}$
a_{4i}	$-6.03348\cdot10^{-10}$	$5.57791\cdot10^{-12}$	$-1.72577\cdot10^{-14}$	$1.77978\cdot10^{-17}$

Parameters used in (B.45)-(B.46) are given in Table B.8 and for the expression for the volume of water (B.46b), coefficients are listed in Table B.9.

For the empty hydrate lattice, $g_{w_0,\beta}$ is the molar Gibbs energy of formation of the standard hydrate at reference conditions. Molar enthalpy $h_{w,\beta}$ and molar volume $v_{w,\beta}$ are given by:

$$h_{w,\beta} = h_{w_0,\beta} + \int_{T_0}^{T} c_{P_{w,\beta}}\, dT \tag{B.48a}$$

$$v_{w,\beta} = v_0 \exp[\alpha_1 \Delta T + \alpha_2 \Delta T^2 + \alpha_3 \Delta T^3 - \kappa(P - P_0)] \tag{B.48b}$$

where ΔT is defined as $(T - T_0)$ and the heat capacity of the standard sI hydrate at reference pressure is well approximated by that of ice (Ballard, 2002) and written in the same form as (B.47). Parameters used in (B.48) are listed in Table B.10.

Table B.10: Parameters used in (B.48)

$g_{w_0,\beta}$	$h_{w_0,\beta}$	a_0/R	a_1/R	a_2/R	a_3/R
-235537.85	-291758.77	0.735409713	$1.4180551\cdot10^{-2}$	$-1.72746\cdot10^{-5}$	$63.5104\cdot10^{-9}$
v_0	α_1	α_2	α_3	κ	
22.7712	$3.384960\cdot10^{-4}$	$5.400990\cdot10^{-7}$	$-4.769460\cdot10^{-11}$	$3.0\cdot10^{-5}$	

For the hydrate phase, the energy change is expressed by:

$$\frac{\Delta\mu_{w,H}}{RT} = \frac{\mu_{w,H} - g_{w,\beta}}{RT} = \sum_m v_m \ln\left[1 - \sum_i \theta_{im}\right] \tag{B.49}$$

with v_m the number of cages of type m, divided by the number of water molecules in the hydrate lattice ($v_m = 2/46$ for small 5^{12} cages and $v_m = 6/46$ for large $5^{12}6^2$ cages), and θ_{im} is the fractional occupancy of guest i in cage m. Here, the fractional occupancy will always be a number smaller than 1. Therefore, the natural log will always be a number smaller than zero. That implies that the occupation of cages lowers the total energy of the hydrate. The fractional occupancy of guest i is described by a Langmuir type expression as:

$$\theta_{im} = \frac{C_{im} f_{iH}}{1 + \sum_j C_{jm} f_{jH}} \tag{B.50}$$

where f_{iH} denotes the fugacity of the guest, which is taken to be equal to the fugacity of the guest in other phases. Under equilibrium conditions, fugacity of the guest in the hydrate phase is, by definition, always equal to that in other phases. For kinetic conditions, this is not necessarily the case, but the fractional occupancy will be lower for lower guest fugacity and higher for higher guest fugacity; thereby respectively increasing and reducing the fugacity of water in the the hydrate phase through (B.49). Accordingly, dissociation will occur upon low guest fugacity in the V/Aq phase and formation is associated with high guest fugacity in the V/Aq phase, ultimately moving towards equilibrium.

C_{im} is the Langmuir constant describing the potential interaction between encaged guest molecule i and the water molecules in hydrate cage m surrounding it. It is evaluated by a spherically symmetrical potential as

$$C_{im} = \frac{4\pi}{kT} \int_0^{R_m - a_i} e^{-\frac{\omega_{im}(r)}{kT}} r^2\, dr \tag{B.51}$$

where R_m is the radius of cage m and $\omega_{im}(r)$ is the potential function. Following Ballard (2002), the Kihara spherical core potential is used to calculate the Langmuir constants, leading to:

$$\omega_{im}(r) = 2\epsilon_i z_m \left[\frac{\sigma_i^{12}}{R_m^{11} r} \left(\delta_{im}^{10} + \frac{a_i}{R_m} \delta_{im}^{11} \right) - \frac{\sigma_i^6}{R_m^5 r} \left(\delta_{im}^4 + \frac{a_i}{R_m} \delta_{im}^5 \right) \right] \tag{B.52}$$

where z_m is the number of water molecules comprising cavity m, and a_i, ϵ_i and σ_i are the hard-core radius, potential well depth, and soft-core radius of guest i in hydrate cage m, respectively, and

$$\delta_{im}^N = \frac{1}{N} \left[\left(1 - \frac{r}{R_m} - \frac{a_i}{R_m} \right)^{-N} - \left(1 + \frac{r}{R_m} - \frac{a_i}{R_m} \right)^{-N} \right] \tag{B.53}$$

For R_m, an approximation is to take the average radius of each cage (Ballard, 2002). For the sI type hydrate, the small 5^{12} cage has an average radius of 3.908 A with a number of 20 water molecules surrounding the guest ($= z_m$). The large $5^{12}6^2$ cage has an average radius of 4.326 A with a number of 24 water molecules. The guest-specific parameters for equations (B.51)-(B.53) are listed in Table B.11.

Table B.11: Guest-specific parameters for equations (B.51)-(B.53)

	a_i [A]	σ_i [A]	ϵ/k [K]
CH_4	0.3834	3.14393	155.593
CO_2	0.6805	2.97638	175.405
N_2	0.3526	3.13512	127.426

In the kinetic reaction, we simplify the stoichiometry to be always equal to 5.75, corresponding to full cage occupancy. This assumption may be relaxed later on.

B.2.3. Normalization

In the flash procedure, composition must be normalized in order to obtain the required results. Salt mole fractions must not be taken into account (only salt molality) and under kinetic conditions, the hydrate component must be excluded from phase behaviour entirely. After flash, mole fractions must be re-normalized to find the actual partitioning of components among the phases considered.

Hydrate Under kinetic conditions, composition must be normalized in order to exclude mole fractions of the hydrate component from flash calculations:

$$z_i^* = z_i / \left(1 - z_{\text{Hydrate}} \right) \qquad \text{for i} \neq \text{Hydrate} \tag{B.54}$$

After flash results, overall mole fractions must be re-normalized according to:

$$z_i = z_i^* \cdot \left(1 - z_{\text{Hydrate}} \right) \tag{B.55}$$

and hydrate phase fraction H is equal to hydrate composition z_{Hydrate}, as the hydrate component is the only component occupying hydrate phase H. Then, other phase fractions must be re-normalized in order to allow for the hydrate phase fraction according to:

$$v_j = v_j^* \cdot \left(1 - H \right) \qquad \text{for j} \neq \text{H} \tag{B.56}$$

Phase mole fractions remain the same, as the phase mole fraction of the hydrate component is equal to zero in each non-hydrate phase.

Salt Mole fractions of salt are not taken into account in negative flash calculations. Mole fractions must be normalized before running flash and re-normalized afterwards.

For normalization, a similar procedure as used in hydrate normalization (B.54) is carried out, but then excluding NaCl from composition.

$$z_i^{**} = z_i^* / \left(1 - z_{\text{NaCl}} \right) \qquad \text{for i} \neq \text{NaCl, Hydrate} \tag{B.57}$$

After flash results, re-normalization in order to include salt in the mole fractions can be realized according to:

$$\begin{aligned} v_j &= v_j^* \cdot \left(1 - z_{\mathrm{NaCl}}\right) && \text{for j} \neq \text{H} \\ v_{Aq} &= v_{Aq} + z_{\mathrm{NaCl}} \\ x_{\mathrm{NaCl},Aq} &= z_{\mathrm{NaCl}} / v_{Aq} \\ x_{i,Aq} &= x_{i,Aq} \cdot \left(1 - x_{\mathrm{NaCl},Aq}\right) && \text{for i} \neq \text{NaCl} \end{aligned} \tag{B.58}$$

B.3. Flow properties

B.3.1. Permeability and relative permeability

The change in absolute permeability with hydrates present is quantified by (3.14). As CH_4-brine and CO_2-brine systems exhibit slightly different behaviour, parameters are given for both cases in Table B.12. Permeability for hydrate saturation of zero (that is, with absolute porosity ϕ_0) reduces to absolute permeability k_0.

Table B.12: Fitting parameters for absolute permeability reduction (3.14)

	k_0	ϕ_0	ϕ_c	n
CH_4-brine	1.5 D	0.24	0.07	1.7
CO_2-brine	1.5 D	0.24	0.10	2.3

Then, relative permeability for fluid phases with both zero and nonzero hydrate saturation is expressed by the Brooks-Corey relation in (3.15) and (3.16). The parameters for these equations [3, 17] for both cases used in a CH_4-brine system and a CO_2-brine system are listed in Table B.13.

Table B.13: Fitting parameters for relative permeabilities (3.15) and (3.16)

	$k^0_{r,g}$	$k^0_{r,w}$	$s_{g,r}$	$s_{w,c}$	n_g	n_w
CH_4-brine	0.8	0.5	0.20	0.20	2.7	2.0
CO_2-brine	0.8	0.5	0.20	0.20	4.0	2.0
CH_4-brine-H	0.6	0.5	0.30	0.20	3.6	3.2
CO_2-brine-H	0.6	0.5	0.37	0.20	5.8	3.2

B.4. Thermophysical properties

B.4.1. Density

Aqueous phase In calculating the density of the aqueous phase, only the contribution of salt is taken into account. The contribution of methane to water is neglected, as its solubility in water is relatively low.

The density of brine containing NaCl can be obtained from Spivey [27], given by:

$$\rho_b(P,T,m) = \rho_{b0}(T,m) \exp\left[I_b(P,T,m) - I_b(P_0,T,m)\right] \tag{B.59}$$

where m is the molality of NaCl in the solution [mol/kg], ρ_{b0} represents the density of brine at the reference pressure P_0 of 70 MPa and I_b denotes the coefficient of isothermal compressibility for brine. The reference density reads:

$$\rho_{b0} = \rho_{w0} + D_{b1}(T)m^2 + D_{b2}(T)m^{3/2} + D_{b3}(T)m + D_{b4}(T)m^{1/2} \tag{B.60}$$

where ρ_{w0} denotes the density of pure water at reference pressure. The coefficient of isothermal compressibility for brine reads:

$$I_b(P,T,m) = \int_P c_b \, dP = \frac{1}{E_b(T,m)} \ln\left|E_b(T,m)\left(\frac{P}{P_0}\right) + F_b(T,m)\right| \tag{B.61}$$

Here, coefficient E_b is described by:

$$E_b(T,m) = E_w(T) + E_{b1}(T)m \tag{B.62}$$

and coefficient F_b is calculated as:

$$F_b(T,m) = F_w(T) + F_{b1}(T)m^{3/2} + F_{b2}(T)m + F_{b1}(T)m^{1/2} \tag{B.63}$$

All coefficients D, E and F used in (B.60)-(B.63), as well as the expression for density of pure water at reference pressure ρ_{w0}, take the form of:

$$a(T) = \frac{a_1\left(\frac{T}{100}\right)^2 + a_2\left(\frac{T}{100}\right) + a_3}{a_4\left(\frac{T}{100}\right)^2 + a_5\left(\frac{T}{100}\right) + 1} \tag{B.64}$$

with the coefficients a_i listed in Table B.14. It must be noted that when the molality of salt in the solution is equal to zero, the relation for brine density reduces to that of pure water density at given pressure and temperature.

Table B.14: Parameters for Spivey correlation (B.59)-(B.64)

i	1	2	3	4	5
ρ_{w0}	-0.127213	0.645486	1.03265	-0.070291	0.639589
D_{b1}	$-7.925\cdot10^{-5}$	$-1.93\cdot10^{-6}$	$-3.4254\cdot10^{-4}$	0	0
D_{b2}	$1.0998\cdot10^{-3}$	$-2.8755\cdot10^{-3}$	$-3.5819\cdot10^{-3}$	-0.72877	1.92016
D_{b3}	$-7.6402\cdot10^{-3}$	$3.6963\cdot10^{-2}$	$4.36083\cdot10^{-2}$	-0.333661	1.185685
D_{b4}	$3.746\cdot10^{-4}$	$-3.328\cdot10^{-4}$	$-3.346\cdot10^{-4}$	0	0
E_w	4.221	-3.478	6.221	0.5182	-0.4405
E_{b1}	0	0	0.1353	0	0
F_w	-11.403	29.932	27.952	0.20684	0.3768
F_{b1}	-1.409	-0.361	-0.2532	0	9.216
F_{b2}	0	5.614	4.6782	-0.307	2.6069
F_{b3}	-0.1127	0.2047	-0.0452	0	0

Hydrate phase Density of the hydrate phase can be calculated according to equation proposed by Ballard [4]:

$$\rho_H = M_H / \left[V_0 \exp(3.38496\cdot10^{-4}\Delta T + 5.40099\cdot10^{-7}\Delta T^2 - 4.76946\cdot10^{-11}\Delta T^3 + 3\cdot10^{-5}\Delta P) \right] \tag{B.65}$$

where $\Delta T = T - T_0$ and $\Delta P = P - P_0$ with T_0 = 298.15 K and P_0 = 1 bar. Specific volume [cm^3 mol^{-1}] at reference temperature and pressure is given as V_0 = 22.712, with M_H the average molecular weight of the hydrate.

B.4.2. Viscosity

Vapour phase The method of Lee [15] gives viscosity of typical natural gas mixtures with low non-hydrocarbon content according to:

$$\mu_v = 1\cdot10^{-4} K \exp\left[X\cdot\left(\frac{\rho_v}{62.4}\right)^Y \right] \tag{B.66}$$

where vapour mass density ρ_v is given in [lbs/ft^3]. Parameters K, X and Y are calculated by:

$$K = \frac{\left(9.4 + 0.02M_v\right)T^{1.5}}{209 + 19M_v + T} \tag{B.67}$$

$$X = 3.5 + \frac{986}{T} + 0.01M_v \tag{B.68}$$

$$Y = 2.4 - 0.2X \tag{B.69}$$

where T is in Rankine scale and M_v denotes the average molar mass of the gas mixture.

Aqueous phase Mao [18] developed a relation for the viscosity of pure water as:

$$\ln\mu_{\mathrm{H_2O}} = \sum_{i=1}^{5} d_i T^{i-3} + \sum_{i=6}^{10} d_i \rho_{\mathrm{H_2O}} T^{i-8} \tag{B.70}$$

with $\mu_{\mathrm{H_2O}}$ in [Pa·s], pure water density as calculated in Appendix B.4.1 and coefficients d_i given in Table B.15.

Table B.15: Coefficients used for (B.70)

d_1	d_2	d_3	d_4	d_5
$0.28853170 \cdot 10^{7}$	$-0.11072577 \cdot 10^{5}$	$-0.90834095 \cdot 10^{1}$	$0.30925651 \cdot 10^{1}$	$-0.27407100 \cdot 10^{-4}$
d_6	d_7	d_8	d_9	d_{10}
$-0.19283851 \cdot 10^{7}$	$0.56216046 \cdot 10^{4}$	$0.13827250 \cdot 10^{2}$	$-0.47609523 \cdot 10^{-1}$	$0.35545041 \cdot 10^{-4}$

Mao [18] derived a relation for the relative viscosity μ_r; that is, the ratio between the viscosity of the saline solution and pure water:

$$\mu_r = \frac{\mu_{H_2O-NaCl}}{\mu_{H_2O}} \tag{B.71}$$

where

$$\ln \mu_r = Am + Bm^2 + Cm^3 \tag{B.72}$$

Here, m is the molality of salt [mol kg^{-1}]. The coefficients A, B and C are functions of temperature according to:

$$A = a_0 + a_1 T + a_2 T^2 \tag{B.73a}$$

$$B = b_0 + b_1 T + b_2 T^2 \tag{B.73b}$$

$$C = c_0 + c_1 T \tag{B.73c}$$

Coefficients a_i, b_i and c_i are listed in Table B.16. Extension to brines containing multiple salt components is discussed in Mao [18], but is not considered here. It must be noted that when the molality of salt in the solution is equal to zero, the relation for brine viscosity reduces to that of pure water viscosity at given pressure and temperature as given by (B.70).

Table B.16: Coefficients used for (B.73)

	0	1	2
a	-0.21319213	$0.13651589 \cdot 10^{-2}$	$-0.12191756 \cdot 10^{-5}$
b	$0.69161945 \cdot 10^{-1}$	$-0.27292263 \cdot 10^{-3}$	$0.20852448 \cdot 10^{-6}$
c	$-0.25988855 \cdot 10^{-2}$	$0.77989227 \cdot 10^{-5}$	

B.4.3. Phase thermal properties

Enthalpy For the vapour phase, specific enthalpy is computed as

$$h_V = \sum_i x_{iV} h_{iV} + h_{dep} \tag{B.74}$$

where h_{ij} is the specific enthalpy of component i in the vapour phase and h_{dep} is the enthalpy departure, which is calculated from Peng-Robinson EoS [22]. This quantity is defined as the difference between the enthalpy of the vapour phase h and its enthalpy as computed for an ideal gas $h*$. It is related to Z (B.19) as:

$$h - h* = RT(Z-1) + \frac{T\frac{da}{dT} - a}{2\sqrt{2}b} \ln\left(\frac{Z + 2.414B}{Z - 0.414B}\right) \tag{B.75}$$

In our calculations, we simplify such that only CH_4 in vapour is accounted for in the summation term and in the enthalpy departure. Then, specific enthalpy of CH_4 is equal to:

$$h_{CH_4,V} = \int_{T_0}^{T} c_{P,CH_4}\, dT \tag{B.76}$$

In this work, c_{P,CH_4} is taken as constant over the range of pressure and temperature, reducing (B.76) to $h_{CH_4,V} = c_{P,CH_4}(T - T_0)$. The constant pressure heat capacity for CH_4 can be found in Table B.17. For the aqueous phase, specific enthalpy is given by the enthalpy of pure water, as described by (B.46). The specific enthalpy of hydrate phase is taken to be the standard hydrate molar enthalpy as (B.48).

Internal energy Phase specific internal energy is related to enthalpy according to:

$$U_j = h_j - PV_m = h_j - P/\rho_j \tag{B.77}$$

where h_j is calculated in according to the previous paragraph and ρ_j denotes the molar density of the phase, as described in Appendix B.4.1. Rock specific internal energy is calculated as:

$$U_r = \int_{T_0}^{T} c_{vr}\, dT \tag{B.78}$$

where c_{vr} denotes the heat capacity of the rock matrix at constant volume. In this work, c_{vr} is taken as constant over the range of pressure and temperature, reducing (B.78) to $U_r = c_{vr}(T - T_0)$. Its value can be found in Table B.17.

Thermal conductivity The composite thermal conductivity of the medium-fluid ensemble as described by Yin [30] reads:

$$\overline{\kappa} = \kappa_d + \left(s_{Aq}^{1/2} + s_H^{1/2}\right)\left(\kappa_w - \kappa_d\right) \tag{B.79}$$

where subscripts d and w refer to thermal conductivity of sand under dry and fully saturated conditions, respectively. Values for κ_d and κ_w are listed in Table B.17.

Table B.17: Thermal parameters used in (B.74)-(B.79)

Parameter		Unit
$c_{P,\mathrm{CH_4}}$	$35.8{\cdot}10^{-3}$	kJ mol^{-1} K^{-1}
c_{vr}	3710	kJ m^{-3} K^{-1}
κ_d	$0.30{\cdot}10^{-3}$	kJ s^{-1} m^{-1} K^{-1}
κ_w	$1.65{\cdot}10^{-3}$	kJ s^{-1} m^{-1} K^{-1}

B.4.4. Hydrate formation and dissociation reactions

The kinetic reaction rate is described by (3.17). Here, the kinetic rate parameters are taken from Yin [30]. Reaction surface area A_s is described by Moridis [20]:

$$A_s = 0.879 F_A(t) \frac{1-\phi}{r_p} s_H^{2/3} \tag{B.80}$$

where $F_A(t)$ is the surface area adjustment factor, optimized as a function of time based on history matching (here, $F_A = 1$), and solid grain radius r_p reads:

$$r_p = \left[45k \frac{(1-\phi)^2}{\phi^3}\right]^{1/2} \tag{B.81}$$

For the kinetic rate constant K, a value of $3.6{\cdot}10^4$ kg m^{-2} Pa^{-1} s^{-1} is often used in literature [30], which corresponds to $3.11{\cdot}10^{14}$ mol m^{-2} bar^{-1} day^{-1}. Here, it must be noted that this corresponds to a reaction rate that is driven by the difference in hydrate guest (CH_4) fugacity. However, in our model, the reaction is driven by the difference in H_2O fugacity between hydrate and other phases ($f_{w,H} - f_{w,Aq}$), which is several orders of magnitude smaller. Therefore, K must be several orders of magnitude higher to correct for this:

$$K = 5 \cdot 10^{17} \text{ mol m}^{-2} \text{ bar}^{-1} \text{ day}^{-1}$$

History matching with experimental results will have to provide more accurate values. The calculation of fugacity of water in the hydrate phase and the fugacity of water in the aqueous phase is described in Appendix B.2.2.

C

Graphical presentation of models

C.1. Phase behaviour

C.1.1. Methane solubility in aqueous phase

The solubility of methane in the aqueous phase based on the fugacity models [22, 32] has been visualized in terms of aqueous phase mole fraction in Figure C.1. The solubility of methane in the range of this study has been shown in Figure C.2. However, care should be taken when the activity model is extrapolated to temperatures below 5°C (see Section 5).

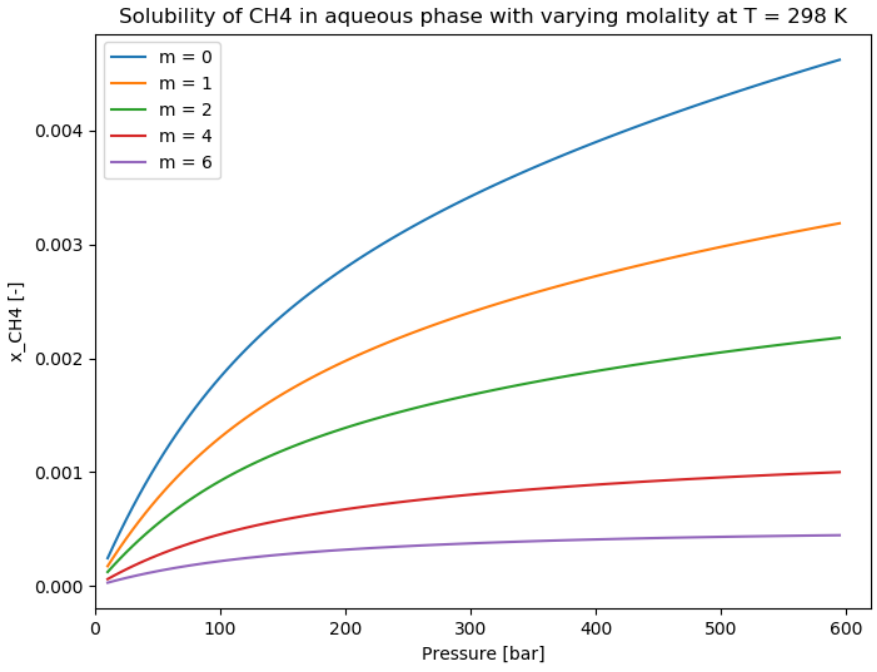

Figure C.1: Methane aqueous phase fraction with molality from study of Ziabaksh [32], calculated with activity model and Peng-Robinson [22]

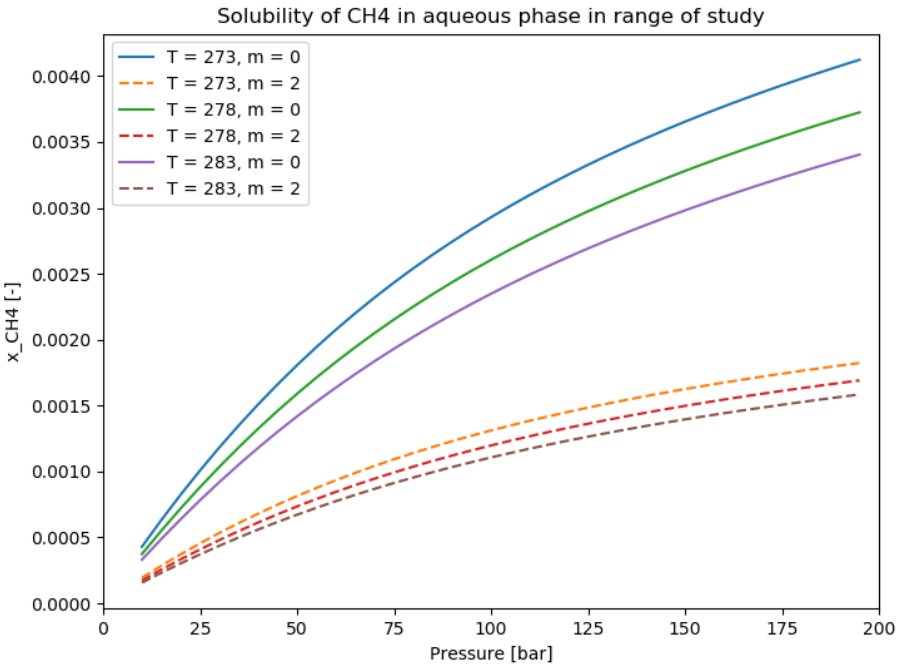

Figure C.2: Methane aqueous phase fraction in range of study, calculated with activity model from Ziabaksh [32] and Peng-Robinson [22]

C.1.2. Water vapour fraction

The water vapour phase mole fraction in range of study, calculated with activity model from Ziabaksh [32] and Peng-Robinson [22], has been displayed in Figure C.3.

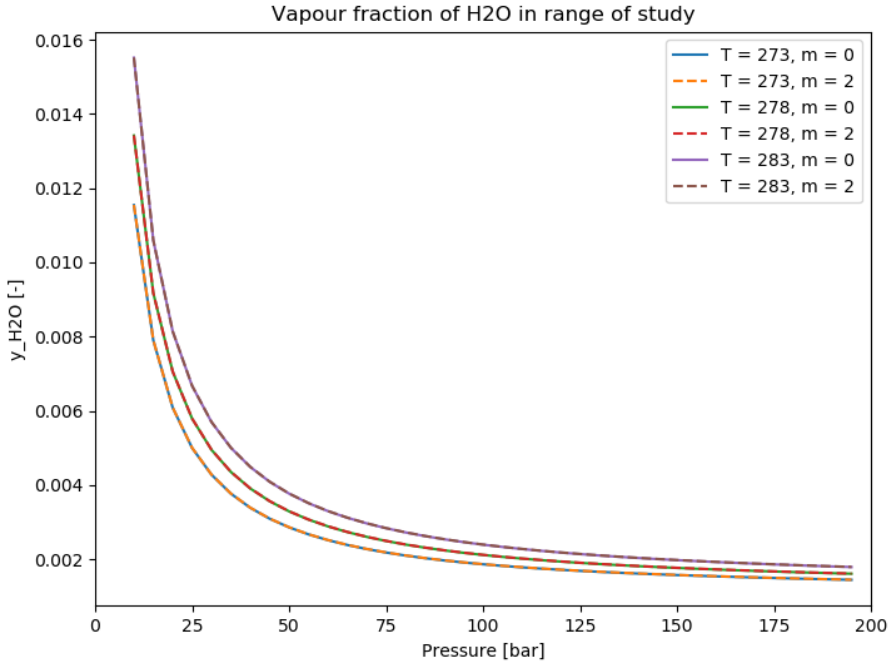

Figure C.3: Water vapour phase mole fraction in range of study, calculated with activity model from Ziabaksh [32] and Peng-Robinson [22]

C.2. Thermophysical properties

C.2.1. Density

Vapour phase The mass density of a pure-CH_4 vapour phase, calculated from the Peng-Robinson EoS [22], is shown in Figure C.4.

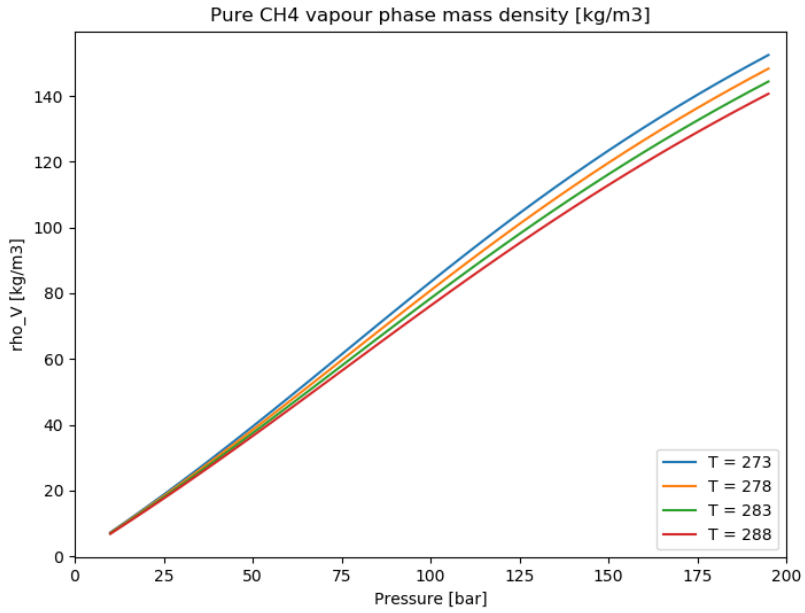

Figure C.4: Pure-CH_4 vapour phase mass density, calculated from Peng-Robinson EoS [22]

Aqueous phase The mass density of the aqueous phase with varying salt molality, calculated from Spivey [27], is shown in Figure C.5. The effect of dissolved CH_4 is neglected here (see Section 3.2.1).

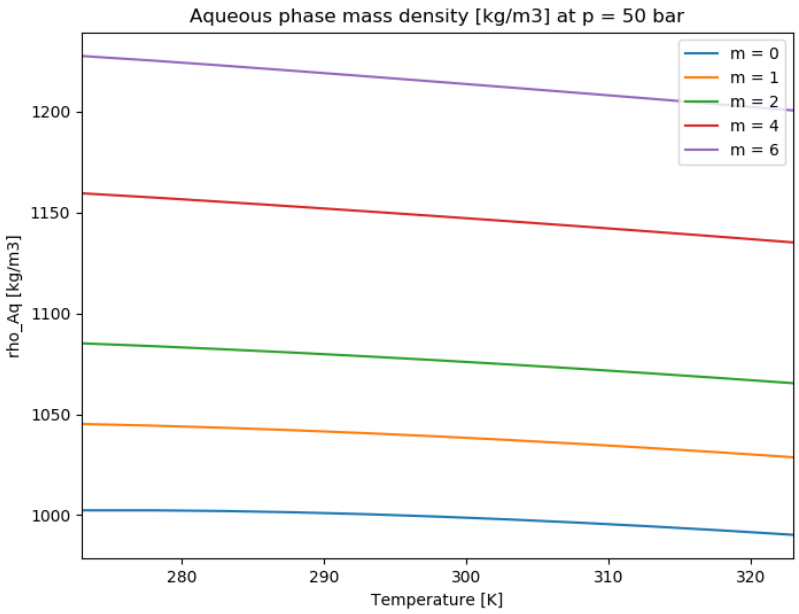

Figure C.5: Mass density of the aqueous phase with varying salt molality, calculated from Spivey [27]

Hydrate phase The mass density of the hydrate phase, calculated from Ballard [4], is shown in Figure C.6.

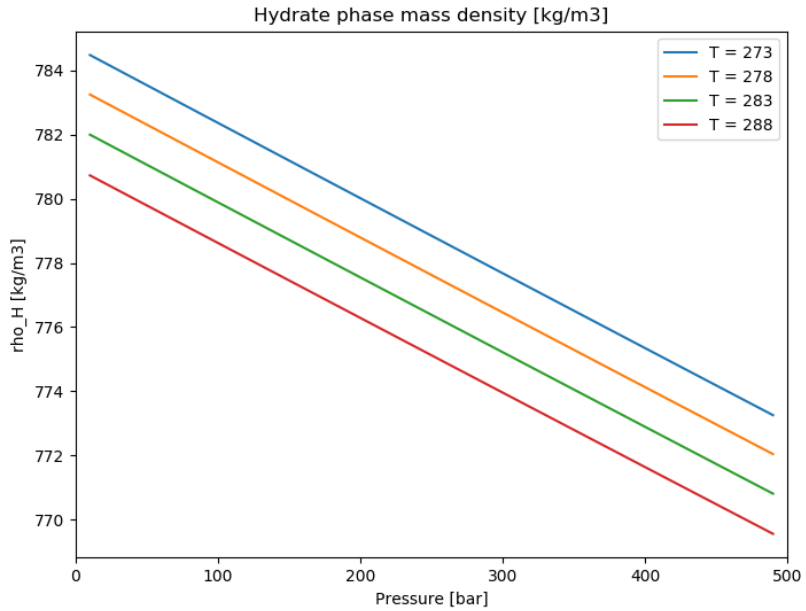

Figure C.6: Mass density of the hydrate phase, calculated from Ballard [4]

C.2.2. Viscosity

Vapour phase The viscosity of the vapour phase is calculated from Lee [15]. This correlation is valid for typical natural gas mixtures with low non-hydrocarbon content, however it has been developed for slightly higher temperatures (T> 35°C), so care should be taken when extrapolating to lower temperatures. Viscosity for the specified range of p-T from Lee [15] has been shown in C.7. Viscosity of a pure-CH_4 vapour phase over the range of temperature and pressure of interest for this study has been displayed in Figure C.8.

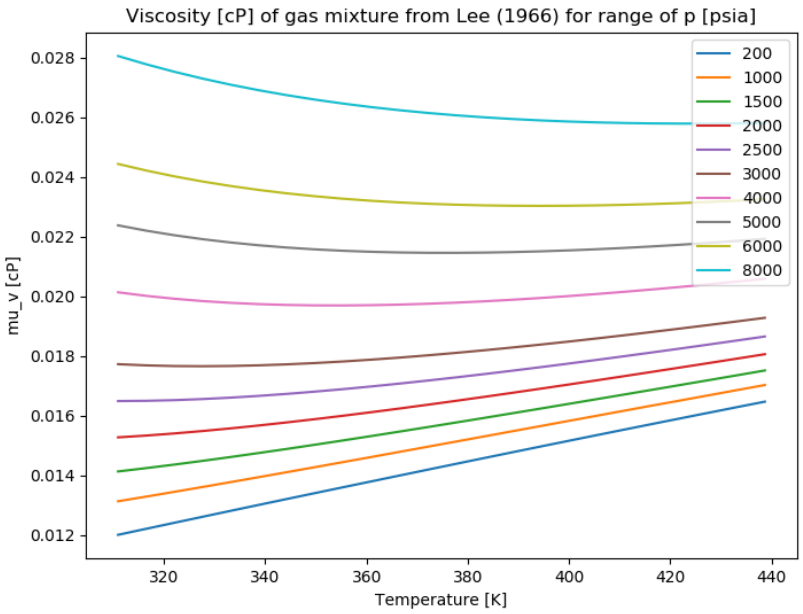

Figure C.7: Viscosity of gas mixture given Lee [15] for specified range of p-T in [15]. [N2, CO2, CH4]: [0.0059, 0.0181 0.9760]

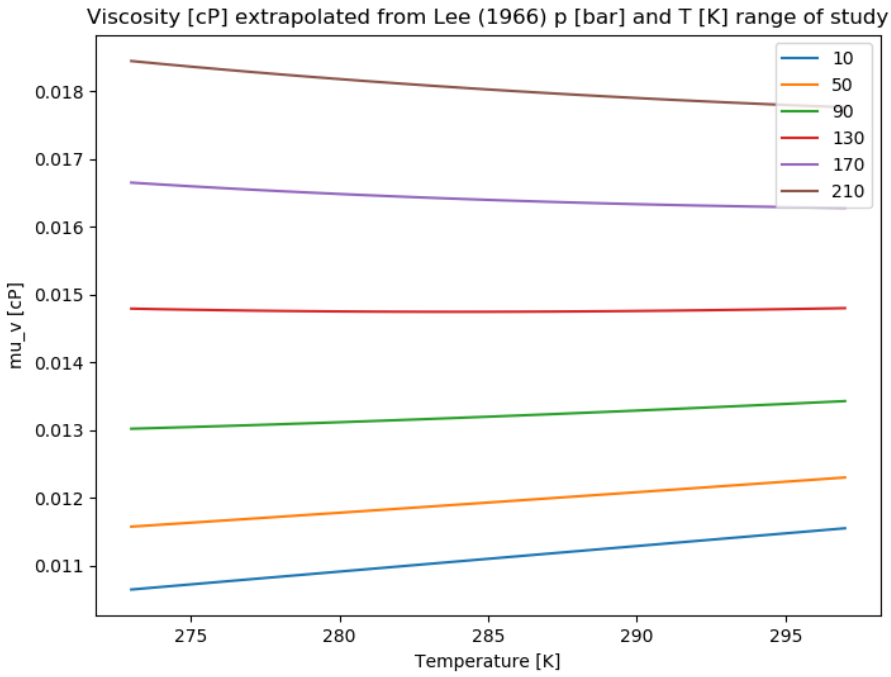

Figure C.8: Viscosity of a pure-CH_4 vapour phase over the range of temperature and pressure of interest for this study, from Lee [15]

Aqueous phase The viscosity of aqueous electrolyte solutions depends strongly on temperature, less on salinity, and is much less dependent on pressure, according to Mao [18]. Viscosity of the aqueous phase with varying temperature and salt molality, calculated from Mao [18], is shown in Figure C.9.

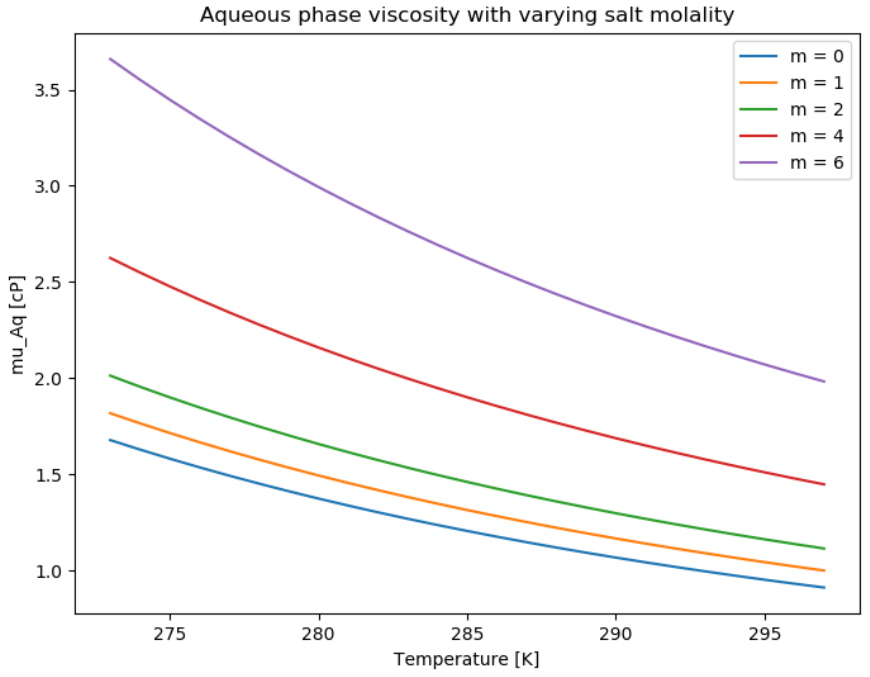

Figure C.9: Viscosity of the aqueous phase with varying temperature and salt molality, calculated from Mao [18]